arXiv:1610.04818v1 [cond-mat.str-el] 16 Oct 2016

Staggered Flux State in Two-Dimensional Hubbard Models

Hisatoshi Yokoyama*,[1] Shun Tamura[2], and Masao Ogata[3]

[1]*Department of Physics, Tohoku University, Sendai 980-8578, Japan*
[2]*Department of Applied Physics, Nagoya University, Nagoya 464-8603, Japan*
[3]*Department of Physics, University of Tokyo, Bunkyo-ku, Tokyo 113-0033. Japan*

The stability and other properties of a staggered flux (SF) state or a correlated d-density wave state are studied for the Hubbard (t-t'-U) model on extended square lattices, as a low-lying state that competes with the $d_{x^2-y^2}$-wave superconductivity (d-SC) and possibly causes the pseudogap phenomena in underdoped high-T_c cuprates and organic κ-BEDT-TTF salts. In calculations, a variational Monte Carlo method is used. In the trial wave function, a configuration-dependent phase factor, which is vital to treat a current-carrying state for a large U/t, is introduced in addition to ordinary correlation factors. Varying U/t, t'/t, and the doping rate (δ) systematically, we show that the SF state becomes more stable than the normal state (projected Fermi sea) for a strongly correlated ($U/t \gtrsim 5$) and underdoped ($\delta \lesssim 0.16$) area. The decrease in energy is sizable, particularly in the area where Mott physics prevails and the circular current (order parameter) is strongly suppressed. These features are consistent with those for the t-J model. The effect of the frustration t'/t plays a crucial role in preserving charge homogeneity and appropriately describing the behavior of hole- and electron-doped cuprates and κ-BEDT-TTF salts. We argue that the SF state does not coexist with d-SC and is not a 'normal state' from which d-SC arises. We also show that a spin current (flux or nematic) state is never stabilized in the same regime.

1. Introduction

Superconductivity (SC) in underdoped high-T_c cuprates should be understood through the relationship to the pseudogap phase observed for $T_c < T < T^*$, where T_c [T^*] is the superconducting (SC) transition [pseudogap] temperature.[1,2] Because the pseudogap phase appears in the proximity of half filling, it is probably related to Mott insulators[3,4] (precisely, charge-transfer insulators[5]). Experimentally, the pseudogap phase presents various features distinct from an ordinary Fermi liquid.[3,4] (1) A large gap different from the $d_{x^2-y^2}$-wave SC (d-SC) gap opens in the spin degree of freedom near the momenta of $(\pi, 0)$ and $(0, \pi)$. (2) However, the material is conductive and does not have a charge gap. (3) Fragmentary Fermi surfaces, i.e., Fermi arcs[6,7] or hole pockets,[8,9] appear in the zone-diagonal direction near $(\pi/2, \pi/2)$.

The origin of the pseudogap has often been studied as a linkage to d-SC, although it will not be related to SC fluctuation.[10–15] On the other hand, recent experimental studies argued that the pseudogap phase is accompanied by some symmetry-breaking phase transitions at T^*.[2] (1) Time-reversal symmetry breaking[16–19] is claimed from polarized neutron scattering signals at the momentum $(0, 0)$ as well as from the appearance of the Kerr effect. (2) Rotational symmetry breaking (or nematic order) similar to the stripe phase is observed, and the oxygen sites between copper atoms are involved.[2,20] (3) Charge orders or charge density waves are observed in resonant X-ray scattering experiments.[21–23] (4) (π, π)-folded (shadow) bands appear in ARPES spectra, and so forth.[24–27] Note, however, that the thermodynamic properties such as specific heat and spin susceptibility have not provided any evidence of the phase transition. It is also important to study whether a pseudogap and other orders coexist or are mutually exclusive.[15,28–30]

In this context, we study a symmetry-breaking state—a staggered flux (SF) state (sometimes called a d-density wave state)—as a possible pseudogap state for the Hubbard model. We should understand such a state in the context of a doped Mott insulator.[3,4] To respect the strong correlation, we use a variational Monte Carlo (VMC) method,[31] which deals with the local correlation factors exactly and has yielded consistent results for many aspects of cuprates.[32–37] If the pseudogap phenomena are generated by a symmetry-breaking state, it should be more stable than the (symmetry-preserved) ordinary normal state. Also, when a predominant antiferromagnetic (AF) or d-SC state is suppressed for some reason, features of the symmetry-breaking state will manifest themselves. Note that a recent VMC calculation with a band-renormalization effect showed that an AF state is considerably stabilized compared with the d-SC state in a wide region of the Hubbard model.[38]

Since the early years of research on cuprate SCs, the SF state has been studied by many groups from both weak- and strong-correlation sides. In the early studies,[39–45] the main aim was to check whether the SF state becomes the ground state, but it was shown mainly using the t-J model that the SF state yields to other ordered states (AF and d-SC) for any relevant parameters. Later, the SF state was mainly studied as a candidate for a normal state that causes the pseudogap phenomena and underlies d-SC in underdoped cuprates.[46–50]

At half filling, for the Heisenberg model, owing to the SU(2) symmetry, the SF state is equivalent to the d-wave BCS state,[51,52] which has a very low energy[31,32] comparable to that of the AF ground state.[53–55] The t-J model with finite doping was studied using U(1) and SU(2) slave-boson mean-field theories[56–58] and a perturbation theory of Hubbard X operators,[59] which revealed that the SF phase exists in phase diagrams but is restricted to very small doping regions.[58] As a more reliable treatment, VMC calculations[32,43,44,60] showed that the SF state has lower energy than the projected Fermi

pointed out that the δ dependence of the SC condensation energy using the SF state as a normal state becomes domelike[60] but that the SF state tends to be unstable toward phase separation.[61] These VMC results claim that the strongly correlated Hubbard model should have the same features.

For the Hubbard model, SF states have been studied using a phenomenological theory,[62] mean-field theories,[63–65] and more refined renormalization group methods[66,67] from the weak-correlation side. These studies obtained various knowledge of the SF state, but it is still unclear whether or not the SF state is stabilized in the weakly as well as strongly correlated regions. On the other hand, a Gutzwiller approximation study[65] claimed that the SF state is not realized in the Hubbard model. A study using a Hubbard operator approach[68] showed the absence of SF order for a large U/t (= 8) unless an attractive intersite interaction is introduced. A study using a dynamical cluster approximation for a 2×2 cluster[69] argued that the circular-current susceptibility increases in the pseudogap-temperature regime but does not diverge, and there is no qualitative change as U/t and t'/t are varied. A study using a variational cluster approach[70] concluded that the SF phase is not stabilized with respect to the ordinary normal state for a strongly correlated region ($U/t \gtrsim 4$). An extended dynamical-mean-field approximation showed that although the SF susceptibility is enhanced, it is dominated by d-SC and an inhomogeneous phase for $t'/t = 0$.[71] Thus, it is still unclear whether the results in the Hubbard model are consistent with those in the t-J model.

The purpose of this paper is to show that the SF state becomes considerably stable with respect to the projected Fermi sea (an ordinary normal state) in the underdoped regime for large values of U/t and $t'/t \sim -0.3$ in the Hubbard (t-t'-U) model, and to clarify various properties of this state on the basis of systematic VMC calculations. It is essential to introduce a configuration-dependent phase factor to treat a current-carrying state such as the SF state in the regime of Mott physics.[72] Without it, the SF state is never stabilized in models permitting double occupation such as the Hubbard model. We change the model parameters U/t, t'/t, and the doping rate δ (= $1 - N/N_{\rm s}$) in a wide range, with N and $N_{\rm s}$ being the numbers of electrons and sites, respectively. Additionally, we study the spin-current flux phase (sometimes called the spin-nematic phase) using the same method.

Besides cuprates, we consider a model for layered organic conductors, κ-(BEDT-TTF)$_2$X, [henceforth, abbreviated as κ-(ET)$_2$X] with X being a univalent anion.[73–75] In these compounds, SC arises for $T_{\rm c} \lesssim 12$ K, and a pseudogap behavior similar to that of cuprates has been observed. Therefore, we need to check whether its origin is identical to that of cuprates. Various low-energy properties of κ-(ET)$_2$X are considered to be described by the Hubbard model[76] on an anisotropic two-dimensional triangular lattice. The value of U/t can be controlled by applying pressure. U is estimated as $U \sim W$–$2W$ with W being the band width.[73] The degree of frustration t'/t can be varied by substituting X or applying uniaxial pressure. t'/t is estimated by ab initio calculations as 0.4–0.7 for weakly frustrated compounds and ~ 0.8 for the highly frustrated compound κ-(ET)$_2$Cu$_2$(CN)$_3$.[73,77] Among the former compounds, deuterated κ-(ET)$_2$Cu[N(CN)$_2$]Br ($t'/t \sim 0.4$) under applied pressure has been shown to exhibit pseudogap behavior such

($1/T_1T$) in the metallic phase ($T > T_{\rm c}$). On the other hand, κ-(ET)$_2$Cu$_2$(CN)$_3$, which has a spin liquid state in the insulating phase under ambient pressure, exhibits the Korringa relation ($1/T_1T$ = const.) in the metallic phase under pressure, namely, pseudogap behavior is absent.[78] Furthermore, similar pseudogap behavior was observed in a hole-doped κ-ET salt [κ-(ET)$_4$Hg$_{2.89}$Br$_8$],[79] in which the doping rate is 0.11 and $t'/t \sim 0.8$. With these experimental results in mind, we study the SF state on an anisotropic triangular lattice in the framework applied to the frustrated square lattice for cuprates.

This paper is organized as follows. In Sect. 2, we introduce the model and method used in this paper. In Sects. 3 and 4, we discuss the results mainly for the simple square lattice ($t' = 0$) at half filling and in doped cases, respectively, to grasp the common properties of the SF state. Section 5 is assigned to the effect of the diagonal hopping term t' for the frustrated square lattice and anisotropic triangular lattice. In Sect. 6, we discuss the results. In Sect. 7, we recapitulate this work. In Appendix A, we summarize the fundamental features of the noninteracting SF state. In Appendix B, we briefly review the stability of the SF phase for t-J-type models with new accurate data. In Appendix C, we show that the spin current (flux) state is unstable toward the projected Fermi sea in t-J-type models for any J (> 0) and δ. Preliminary results on the effect of t' terms have been reported in two preceding publications.[80,81]

2. Model and Wave Functions

In Sects. 2.1 and 2.2, we explain the model and variational wave functions used in this paper, respectively. In Sect. 2.3, we introduce a phase factor essential for treating a current-carrying state in a strongly correlated regime. In Sect. 2.4, we describe the numerical settings of our VMC calculations.

2.1 Hubbard model

As models of cuprates and κ-ET organic conductors, we consider the following Hubbard model ($U \geq 0$) on extended square lattices (Fig. 1):

$$\begin{aligned} \mathcal{H} &= \mathcal{H}_{\rm kin} + \mathcal{H}_U \\ &= -\sum_{(i,j),\sigma} t_{ij}\left(c^{\dagger}_{i\sigma}c_{j\sigma} + {\rm H.c.}\right) + U\sum_{j} n_{j\uparrow}n_{j\downarrow}, \end{aligned} \quad (1)$$

where $n_{j\sigma} = c^{\dagger}_{j\sigma}c_{j\sigma}$ and (i, j) indicates the sum of pairs on sites i and j. In this work, the hopping integral t_{ij} is t for nearest neighbors (≥ 0), t' for diagonal neighbors, and 0 otherwise ($\mathcal{H}_{\rm kin} = \mathcal{H}_t + \mathcal{H}_{t'}$) for the two lattices shown in Fig. 1. The bare energy dispersions are

$$\epsilon_{\mathbf{k}} = \begin{cases} -2t\left(\cos k_x + \cos k_y\right) - 4t' \cos k_x \cos k_y, & \text{(a)} \\ -2t\left(\cos k_x + \cos k_y\right) - 2t' \cos\left(k_x + k_y\right). & \text{(b)} \end{cases} \quad (2)$$

In the following, we use t and the lattice spacing as the units of energy and length, respectively.

We refer to the former (latter) lattice as a frustrated square (anisotropic triangular) lattice for convenience. The effective values of t'/t are considered to be -0.4–-0.1 (~ 0.3) in hole-doped (electron-doped) cuprates.[3,82] For the organic compounds, t'/t is 0.4–0.8. Hubbard models have been extensively studied, and we have shown that a first-order Mott transition occurs at $U = U_{\rm c} \sim W$ at half filling for nonmagnetic

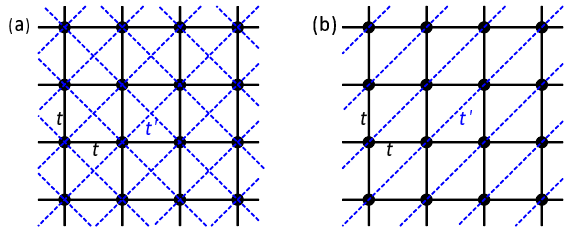

Fig. 1. (Color online) Lattice connectivity or hopping paths in extended square lattice addressed in this study. (a) Frustrated square lattice for cuprate SCs. (b) Anisotropic triangular lattice for organic κ-ET salt SCs. At lattice points (solid circles), onsite repulsion U acts.

near half filling.[33–35] In this paper, we show that similar Mott physics appears in the SF states. It has been shown that, in a wide range of the parameter space of concern, a d-SC state becomes stable compared with the projected Fermi sea (ordinary normal state).[35]

2.2 *Trial wave functions*

We follow many-body variation theory using Jastrow-type trial wave functions: $\Psi = \mathcal{P}\Phi$, where $\mathcal{P}$ indicates a product of many-body projection (Jastrow) factors discussed later and Φ is a mean-field-type one-body wave function.

As a normal (paramagnetic) and reference state, we use a projected Fermi sea, $\Psi_{\rm N} = \mathcal{P}\Phi_{\rm N}$, with

$$\Phi_{\rm N}(t_1/t) = \prod_{\mathbf{k}\in\mathbf{k}_{\rm F}(t_1/t),\ \sigma} c^{\dagger}_{\mathbf{k}\sigma}|0\rangle, \tag{3}$$

where t_1/t is a band-adjusting variational parameter independent of t'/t in $\mathcal{H}$ and $\mathbf{k}_{\rm F}(t_1/t)$ denotes a Fermi surface obtained by replacing $\epsilon_{\mathbf{k}}(t')$ in Eq. (2) with $\epsilon_{\mathbf{k}}(t_1)$. It was shown for $\Psi_{\rm N}$[38] that the band-renormalization effect through t_1/t owing to the electron correlation ($\mathcal{P}$) is sizable for $U \gtrsim U_{\rm c}$, a finite t'/t, and $\delta \sim 0$.

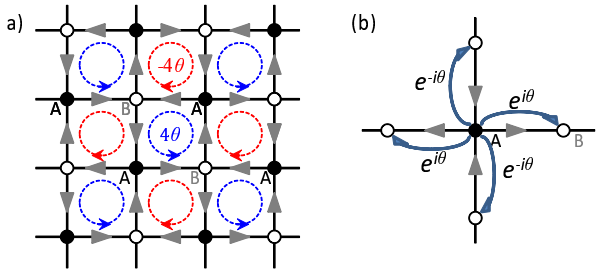

Fig. 2. (Color online) (a) Schematic figure of local current in staggered flux state. Arrows denote the directions of currents. (b) Peierls phase factors attached to hopping terms in $\mathcal{H}^{\rm SF}$ (a case of sublattice A); the sign of the phase depends on the relative directions of the hopping and current.

As a candidate for the pseudogap state, we study a correlated SF state, $\Psi_{\rm SF} = \mathcal{P}\Phi_{\rm SF}$. Here, $\Phi_{\rm SF}$ is the one-body SF state, namely, the ground state of the noninteracting SF Hamiltonian $\mathcal{H}^{\rm SF}$ [shown in Eq. (A·1)], given as

$$\Phi_{\rm SF} = \prod_{\mathbf{k}\in\mathbf{k}_{\rm F},\sigma} \frac{1}{\sqrt{N_{\rm s}}}\left[\sum_{i\in{\rm A}} \Gamma_{\theta,\mathbf{k}} e^{i\mathbf{k}\cdot\mathbf{r}_i} c^{\dagger}_{{\rm A}i\sigma} + \sum_{i\in{\rm B}} e^{i\mathbf{k}\cdot\mathbf{r}_i} c^{\dagger}_{{\rm B}i\sigma}\right]|0\rangle, \tag{4}$$

with

$$\Gamma_{\theta,\mathbf{k}} = \frac{e^{i\theta}\cos k_x + e^{-i\theta}\cos k_y}{\mathcal{S}_{\theta,\mathbf{k}}}, \tag{5}$$

$$\mathcal{S}_{\theta,\mathbf{k}} = \sqrt{\cos^2 k_x + 2\cos 2\theta \cos k_x \cos k_y + \cos^2 k_y}. \tag{6}$$

In $\mathcal{H}^{\rm SF}$, a Peierls phase θ is added to the hopping integrals so that circular current flows in alternate directions in each plaquette as shown in Fig. 2(a). In the present variational theory, θ is a variational parameter to be optimized together with the other parameters. Because $\mathcal{H}^{\rm SF}$ breaks time-reversal and lattice-translational symmetries, $\Phi_{\rm SF}$ does not have these symmetries. The lower-band energy dispersion of $\mathcal{H}^{\rm SF}$ is given as

$$E^{\rm SF}_{-}(\mathbf{k}) = -2t\mathcal{S}_{\theta,\mathbf{k}} = -\sqrt{\frac{1+\cos 2\theta}{2}}\sqrt{\varepsilon^2_{\mathbf{k}} + \Delta^2_{\mathbf{k}}}, \tag{7}$$

with

$$\varepsilon_{\mathbf{k}} = -2t(\cos k_x + \cos k_y), \tag{8}$$

$$\Delta_{\mathbf{k}} = \Delta_\theta(\cos k_x - \cos k_y), \tag{9}$$

and $\Delta_\theta = 2t\sqrt{(1-\cos 2\theta)/(1+\cos 2\theta)}$. Equation (7) is similar to the quasiparticle dispersion of the d-wave BCS wave function. Note that some important features of the bare $\Phi_{\rm SF}$ (summarized in Appendix A) survive in $\Psi_{\rm SF} = \mathcal{P}\Phi_{\rm SF}$. We do not consider Band-renormalization effects on $\Psi_{\rm SF}$ because those due to diagonal currents or hopping are known to raise the variational energy for typical cases.[83]

The correlation factor $\mathcal{P}$ is defined as

$$\mathcal{P} = \mathcal{P}_\phi\, \mathcal{P}_{\rm Q}\, \mathcal{P}_{\rm G}. \tag{10}$$

Here, $\mathcal{P}_{\rm G}$ is the fundamental onsite (Gutzwiller) projection $\mathcal{P}_{\rm G} = \prod_j [1-(1-g)n_{j\uparrow}n_{j\downarrow}]$[84] and $\mathcal{P}_Q$ is an asymmetric projection between a nearest-neighbor doubly occupied site (doublon) and an empty site (holon),[35,85,86]

$$\mathcal{P}_Q = \prod_j \left[1 - \zeta_{\rm d} d_j \prod_\tau \left(1-h_{j+\tau}\right) - \zeta_{\rm h} h_j \prod_\tau \left(1-d_{j+\tau}\right)\right], \tag{11}$$

where $d_j = n_{j\uparrow}n_{j\downarrow}$, $h_j = (1-n_{j\uparrow})(1-n_{j\downarrow})$, and τ runs over the nearest-neighbor sites of site j. g, $\zeta_{\rm d}$, and $\zeta_{\rm h}$ are variational parameters. As shown before,[33,34] the doublon-holon (D-H) binding effect is crucial for appropriately treating Mott physics. At half filling, $\zeta_{\rm d}$ and $\zeta_{\rm h}$ become identical because of the D-H symmetry. In addition to $\mathcal{P}_{\rm G}$ and $\mathcal{P}_Q$, it is vital for the SF state to introduce a phase-adjusting factor $\mathcal{P}_\phi$, which we will explain in the next subsection.

2.3 *Configuration-dependent phase factor*

A current-carrying state is essentially complex, because the current is proportional to $|\Psi|^2\nabla\Theta$, if we represent the state as $\Psi(\mathbf{r}) = |\Psi(\mathbf{r})|e^{i\Theta(\mathbf{r})}$. It is natural that when electron correlation is introduced, the phase part $\Theta(\mathbf{r})$ varies accordingly. However, the conventional correlation factors, $\mathcal{P}_{\rm G}$ and $\mathcal{P}_Q$, are real and do not modify the phase in $\Phi_{\rm SF}$. Therefore, we need to introduce an appropriate phase-adjusting factor into the trial wave function. Such a phase factor was recently introduced for calculating the Drude and SC weights in strongly correlated regimes;[72] thereby, a long-standing problem proposed by Millis and Coppersmith[87]—D-H binding wave functions

insulating regime— was solved.

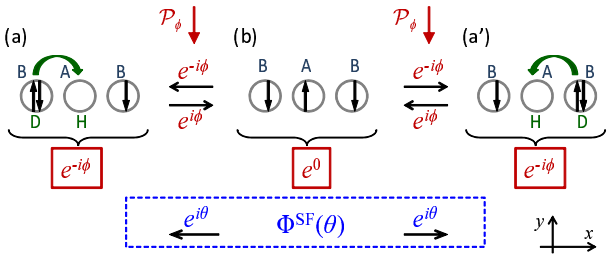

Fig. 3. (Color online) Illustration for assigning configuration-dependent phase ϕ in $\mathcal{P}_\phi$. Here, we assume that an electron hops in the x direction. For the hopping in the y direction, the signs of θ and ϕ have to be reversed. The (Peierls) phase factor assigned by $\Phi_{\rm SF}$ in hopping [Fig. 2(b)] is shown in the blue dashed box. The values in the red boxes are the phase factors in $\mathcal{P}_\phi$ corresponding to the three-site parts shown. The ratio ($e^{\pm\phi}$) indicated by red arrows is produced by $\mathcal{P}_\phi$ in hopping.

We show that this type of phase factor also plays a vital role in the correlated SF state. In $\Phi_{\rm SF}$, a phase θ or $-\theta$ is added when an electron hops to a nearest-neighbor site depending on the direction and position (sublattice), as shown in Fig. 2(b). In the noninteracting case, such hopping occurs equally in all directions. On the other hand, in the strongly correlated regime, the probability of hopping depends on the surrounding configuration (see Fig. 3). For example, when a D-H pair is created [configurations (a) and (a′)], the next hopping occurs probably in the direction in which the singly occupied configuration is recovered [configuration (b)]. This hopping process does not contribute to a global current in the Mott regime ($U \gtrsim U_{\rm c}$).[35] According to a previous study,[72] to reduce the energy, it is important to cancel the phase attached in this type of hopping ($\pm\theta$) by introducing a phase parameter.

This hopping process can be specified by its local configurations and, correspondingly, we can attach a phase-adjusting variational factor to the trial wave function. To be more specific, $\mathcal{P}_\phi$ gives $e^{-i\phi}$ as shown by the solid boxes (red) in Fig. 3, with ϕ being a variational parameter. This phase assignment can be written as

$$\mathcal{P}_\phi = \exp\left[i\phi \sum_{\lambda=1}^{2}(-1)^{\lambda+1}\sum_j d_{\lambda,j} \times \left(h_{\lambda,j+\mathbf{x}} + h_{\lambda,j-\mathbf{x}} - h_{\lambda,j+\mathbf{y}} - h_{\lambda,j-\mathbf{y}}\right)\right], \quad (12)$$

where $\mathbf{x}$ and $\mathbf{y}$ indicate the lattice vectors in the x and y directions, respectively, $\lambda = 1$ ($\lambda = 2$) indicates sublattice A (B), and j runs over all the lattice points in sublattice λ. By $\mathcal{P}_\phi$, a phase factor $e^{\pm i\phi}$ is assigned to a D-H creation or annihilation process, in which $e^{\mp i\theta}$ is yielded by $\Phi_{\rm SF}$ as shown in the dashed box (blue) in Fig. 3. Therefore, when the relation $\phi = \theta$ holds, the total phase shift in a D-H process vanishes.[88] This phase cancelation is acceptable since a phase shift does not appear in an exchange process in the t-J model. On the other hand, the phase is not canceled in the hopping processes unrelated to doublons (or of isolated holons).[89]

The configuration-dependent phase factor $\mathcal{P}_\phi$ is conceptually distinct from position-dependent phase factors used in various contexts.[36,43,90] Note that, without $\mathcal{P}_\phi$, the energy of the SF state is never reduced from that of $\Psi_{\rm N}$ for any model parameters, but $\Psi_{\rm SF}$ with $\mathcal{P}_\phi$ has lower energy than $\Psi_{\rm N}$, as we will see below.[91] Incidentally, this type of phase factor was also recently shown to be crucial for SF states in a Bose Hubbard model[92] and a d-p model.[93] In the regime of Mott physics, the D-H binding affects not only the real part but also the phase in the wave function.

2.4 Variational Monte Carlo calculations

To estimate variational expectation values, we adopt a plain VMC method.[94–97] In this study, we repeat linear optimization of each variational parameter with the other ones being fixed, typically for four rounds of iteration. The linear optimization is convenient for obtaining an energy that is discontinuous in some parameters (θ in this case). After convergence, we continue the same processes for more than 16 rounds and estimate the optimized energy by averaging the data measured in these rounds, excluding excessively scattered data (beyond twice the standard deviation). In each optimization, 2.5×10^5 samples are collected, so that substantially about 4×10^6 measurements are averaged. Only for $\Psi_{\rm SF}$ with $L = 16$ and $\delta = 0$, the sample number is reduced to 2.5×10^4 to save CPU time. Typical statistical errors are $10^{-4}t$ in the total energy and 10^{-4}–2×10^{-3} in the parameters, except near the Mott transition points. We use systems of $N_{\rm s} = L \times L$ sites with $L = 10$–18 under periodic-antiperiodic boundary conditions.

3. Staggered Flux State at Half Filling

First, we study the unfrustrated cases ($t' = 0$) in order to grasp the global features of the SF state because most of them do not change even if t' is introduced. In this section, we focus on the half-filled case.

3.1 Variational energy

Figure 4(a) shows the variational energy per site of $\Psi_{\rm SF}$ measured from that of $\Psi_{\rm N}$,

$$\tilde{E} = E^{\rm SF}(\theta) - E^{\rm N}, \quad (13)$$

as a function of θ for five values of U/t. Here, the variational parameters other than θ are optimized for both $\Psi_{\rm SF}$ and $\Psi_{\rm N}$. The size dependence in the case of $U/t = 12$ is also shown to see the convergence of the values. For $U/t = 6$, $\tilde{E}$ monotonically increases as a function of θ. This behavior is the same for $U/t = 0$ shown in Fig. A·2(b) in Appendix A. Hence, $\Psi_{\rm SF}$ is not stabilized for small values of U/t. The situation changes for $U/t > 6$; $\tilde{E}/t$ becomes considerably negative for finite θ and has a minimum at $\theta/\pi \sim 0.2$ for large values of U/t (= 8–16). This behavior is qualitatively consistent with that of the t-J model, the results of which are summarized in Appendix B for comparison. In Fig. 4(b), we plot the optimized values of the configuration-dependent phase factor ϕ as a function of θ. At the optimized points indicated by arrows, ϕ is very close to θ, especially for large values of U/t. As discussed in Sect. 2.3, the Peierls phase θ in the hopping process is mostly canceled by ϕ. Although θ is canceled out, the state $\Psi_{\rm SF}$ preserves the nature of the original flux state, as shown shortly in Sects. 3.3 and 3.4. That is, a local staggered current flows and the momentum distribution function has a typical $\mathbf{k}$-dependence.

Next, we discuss the U/t dependence of the energy gain of

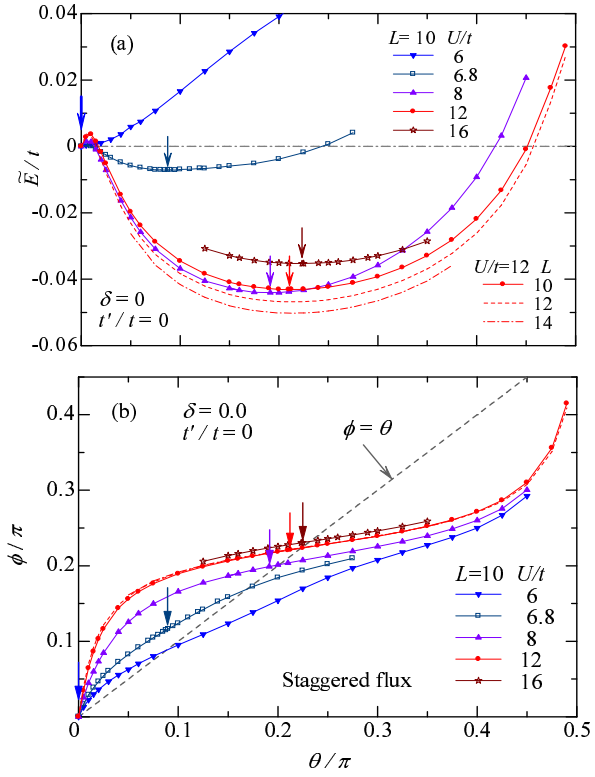

Fig. 4. (Color online) (a) Variational energy per site of the staggered flux state $\Psi_{\rm SF}$ (including $\mathcal{P}_\phi$) measured from that of $\Psi_{\rm N}$ [$E(\theta = 0)$] as a function of θ for several values of U/t ($L = 10$) in the Hubbard model at half filling. Data for $L = 12$ and 14 are added by dashed lines for $U/t = 12$. (b) Optimized phase parameter ϕ for the same values of U/t as in (a). The line of $\phi = \theta$ is added for comparison. The size dependence in (b) is small. In both panels, the arrows indicate the optimal values of θ when $\tilde{E}/t$ is minimum.

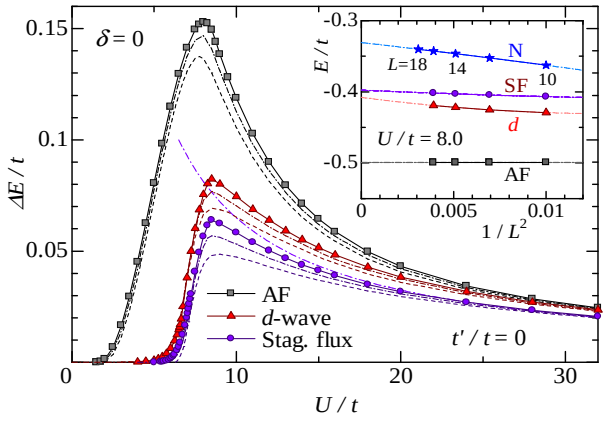

Fig. 5. (Color online) Energy gain of AF, d-SC, and SF states with respect to projected Fermi sea ($\Psi_{\rm N}$) at half filling as functions of U/t. Data for $L = 14$, 12, and 10 for each state are plotted as solid lines with symbols, dash-dotted lines, and dashed lines, respectively. A guide curve proportional to t/U is drawn for ΔE(SF) with $L = 14$ (dash-dotted line). In the inset, the system-size dependence is shown for $U/t = 8.0$ and fitted by second-order polynomials.

the fully optimized $\Psi_{\rm SF}$ with respect to the reference state $\Psi_{\rm N}$,

$$\Delta E(\mathrm{SF}) = E(\mathrm{N}) - E(\mathrm{SF}), \tag{14}$$

where E(N) and E(SF) are the optimized (including θ) energies per site of $\Psi_{\rm N}$ and $\Psi_{\rm SF}$, respectively. If ΔE(SF) is positive, the SF state is stabilized with respect to $\Psi_{\rm N}$. In Fig. 5, we show ΔE(SF) compared with other ordered states, i.e., the AF state, $\Psi_{\rm AF} = \mathcal{P}\Phi_{\rm AF}$, and the d-SC (projected BCS) state, $\Psi_d = \mathcal{P}\Phi_d$. We use the same $\Phi_{\rm AF}$ and Φ_d as in the preceding study (Ref. 35)[98,99] but we adopt Eq. (11) for $\mathcal{P}_Q$. For $\delta = 0$ and $U > U_{\rm c}$, Ψ_d is not SC but Mott insulating. In Fig. 5, each state exhibits a maximum at $U \sim W$ ($= 8t$). The system-size dependence of ΔE for each state is large near the maximum but, as shown in the inset of Fig. 5, ΔE remains finite and the order of the variational energy will not change as $L \to \infty$. ΔE(AF) is largest, i.e., the AF state has the lowest energy for any U/t.[33] For the SF state, ΔE(SF) ~ 0 for small values of U/t ($\lesssim 5$). Although ΔE(SF) is always smaller than ΔE(d−SC), it is close to ΔE(d−SC). At $U/t \sim 5$, ΔE(SF) starts to increase abruptly. The range of U/t where $\Psi_{\rm SF}$ is stabilized ($U/t \gtrsim 5$) is similar to that of Ψ_d. In addition, the behavior of physical quantities such as the momentum distribution function is similar between $\Psi_{\rm SF}$ and Ψ_d as shown shortly. As mentioned, in the Heisenberg model, $\Psi_{\rm SF}(g = 0)$ and $\Psi_d(g = 0)$ are equivalent due to the SU(2) symmetry, but in the Hubbard model, the two states are not equivalent, probably due to the difference in the distribution of doublons and holons.

3.2 *SF transition and Mott transition*

Figure 6 shows the optimized θ and ϕ in $\Psi_{\rm SF}$ as a function of U/t. We find two transition points: $U_{\rm SF}/t$ at $\sim 4-5$ and $U_{\rm c}/t$ at ~ 7. The former corresponds to the SF transition at which $\Psi_{\rm SF}$ starts to have finite θ and ϕ and its variational energy becomes lower than that of $\Psi_{\rm N}$. The latter corresponds to a Mott transition at which the system starts to have a gap in the charge degree of freedom. The symmetry does not change at $U_{\rm c}/t$.

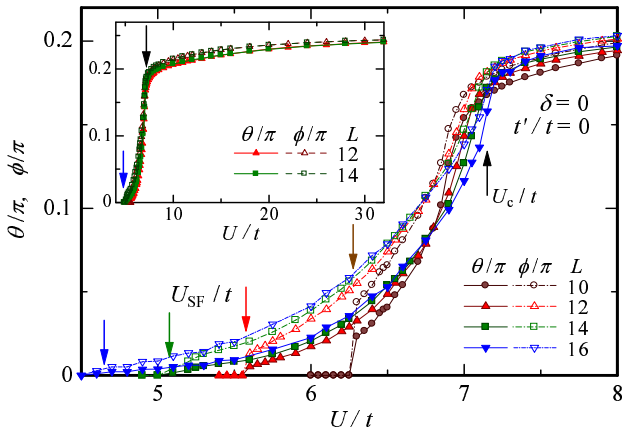

Fig. 6. (Color online) Optimized phase parameters (θ and ϕ) in $\Psi_{\rm SF}$ at half filling. The arrows indicate the Mott transition ($U_{\rm c}/t$) and SF transition ($U_{\rm SF}/t$) for four system sizes. The inset shows the same quantities for a wider range of U/t, with the arrows denoting $U_{\rm c}/t$ and $U_{\rm SF}/t$ for $L = 16$.

At $U_{\rm SF}/t$, θ and ϕ exhibit first-order-transition-like discontinuities, for example, at $U_{\rm SF}/t = 6.28$ for $L = 10$. However, as L increases, $U_{\rm SF}/t$ shifts to lower values and the discontinuities become small and unclear, suggesting that the SF transition is continuous and occurs at a small U/t. Because an appropriate scaling function is not known, we simply perform a polynomial fit of $U_{\rm SF}/t$ up to the square of $1/L^2$ as a

rough estimate. This yields $U_{\rm SF}/t = 2.93$ for $L = \infty$ with a small error. In any case, since θ and ϕ are tiny for $U/t \lesssim 5$, we consider that $\Psi_{\rm SF}$ is substantially not stable in a weakly correlated regime.

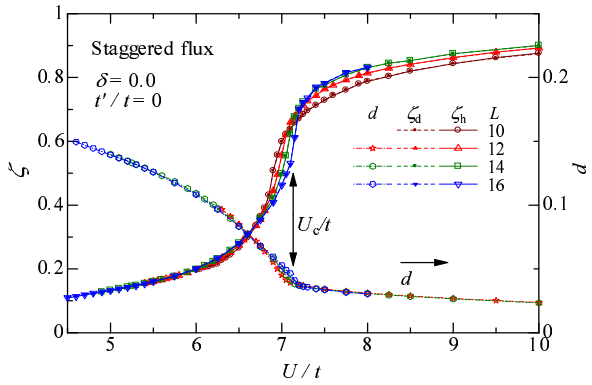

Fig. 7. (Color online) U/t dependences of optimized D-H binding parameter ζ ($= \zeta_{\rm d} = \zeta_{\rm h}$) in $\Psi_{\rm SF}$ and density of doublons d shown at half filling for some system sizes. The arrow indicates the Mott transition point.

Next, we examine the Mott transition at $U_{\rm c}/t$, where the behaviors of θ and ϕ change as shown in Fig. 6. $U_{\rm c}/t = 7.1$ for $L = 16$.[100–102] (Note that in the t-J model, the Mott transition cannot be discussed.) To confirm that $U_{\rm c}/t$ is a Mott transition, we plot the U/t-dependences of the optimized D-H binding parameter ζ ($= \zeta_{\rm d} = \zeta_{\rm h}$) and the doublon density $d = E_U/U$ in Fig. 7. These quantities are sensitive indicators of Mott transitions. In Fig. 7, we find abrupt changes in both ζ and d at $U_{\rm c}/t$, similarly to those in the Mott transitions in Ψ_d and $\Psi_{\rm N}$.[34] In $\Psi_{\rm SF}$, discontinuities in ζ and d at $U_{\rm c}/t$ are not found even for the largest system we treat ($L = 16$). However, because the behavior of both ζ and d becomes more singular as L increases, we consider that this transition is first-order, similarly to those in Ψ_d and $\Psi_{\rm N}$.[34]

3.3 *Spin-gap metal*

In the intermediate regime $U_{\rm SF} < U < U_{\rm c}$, the present SF state is expected to be metallic. In order to clarify the nature of $\Psi_{\rm SF}$, we calculate the momentum distribution function

$$n(\mathbf{k}) = \frac{1}{2}\sum_{\sigma}\langle c^{\dagger}_{\mathbf{k}\sigma}c_{\mathbf{k}\sigma}\rangle \qquad (15)$$

for the optimized $\Psi_{\rm SF}$. Figure 8(a) shows $n(\mathbf{k})$ along the path $(0,0)$-$(\pi,0)$-(π,π)-$(0,0)$ in the original Brillouin zone for various values of U/t. In the region of $U < U_{\rm SF}$ (i.e., $\theta = 0$), we find two discontinuities (crossings of the Fermi surface) at $\mathbf{k} \sim (\pi,0)$ and $(\pi/2,\pi/2)$, indicating a typical Fermi liquid. For $U_{\rm SF} < U < U_{\rm c}$ (half-solid symbols), the discontinuity at $\mathbf{k} \sim (\pi,0)$ disappears, while the discontinuity at $\mathbf{k} \sim (\pi/2,\pi/2)$ remains. This is qualitatively identical to that of the noninteracting SF state $\Phi_{\rm SF}$, in which there is a Dirac point at $(\pi/2,\pi/2)$ and a certain gap opens near the antinodal points. On the other hand, for $U > U_{\rm c}$ (solid symbols), both discontinuities disappear, indicating that a gap opens in the whole Brillouin zone. This is consistent with a Mott insulator.

We can reveal the characters of the gaps to some extent by analyzing the charge density and spin structure factors,

$$N(\mathbf{q}) = \frac{1}{N_{\rm s}}\sum_{i,j} e^{i\mathbf{q}\cdot(\mathbf{R}_i-\mathbf{R}_j)}\left\langle n_i n_j\right\rangle - n^2, \qquad (16)$$

$$S(\mathbf{q}) = \frac{1}{N_{\rm s}}\sum_{ij} e^{i\mathbf{q}\cdot(\mathbf{R}_i-\mathbf{R}_j)}\left\langle S^z_i S^z_j\right\rangle. \qquad (17)$$

On the basis of the single-mode approximation,[103–105] excitations in the charge sector are gapless when $N(\mathbf{q}) \propto |\mathbf{q}|$ for $|\mathbf{q}| \to 0$, whereas a gap opens in the charge sector when $N(\mathbf{q}) \propto |\mathbf{q}|^2$. For $S(\mathbf{q})$, a similar relation holds for the spin sector, although excitations cannot be sharply divided into the charge and spin sectors except for in one-dimensional systems. In Figs. 8(b) and 8(c), $N(\mathbf{q})$ and $S(\mathbf{q})$ are respectively shown for various values of U/t. For $U < U_{\rm SF}$, both $N(\mathbf{q})$ and $S(\mathbf{q})$ behave linearly for $|\mathbf{q}| \to 0$ as expected for a Fermi liquid. For $U > U_{\rm c}$, the behaviors of both $N(\mathbf{q})$ and $S(\mathbf{q})$ appear to be quadratic and consistent with a Mott insulator. For $U_{\rm SF} < U < U_{\rm c}$, $N(\mathbf{q})$ is linear near $(0,0)$, whereas $S(\mathbf{q})$ is quadratic-like,[106] indicating that the state is a spin-gap metal. Namely, the charge and spin sectors show different tendencies in excitation. This feature is distinct from that of the noninteracting SF state $\Phi_{\rm SF}$, which has a gap common to both sectors, and thus $N(\mathbf{q}) = S(\mathbf{q})$ holds (see Appendix A). Therefore, the metallic SF state stable for $U_{\rm SF} < U < U_{\rm c}$ is not perturbatively connected to $\Phi_{\rm SF}$. We will show in the next section that this state is connected to the metallic SF state in the doped case.

3.4 *Circular current*

Now, we turn to the local circular current in a plaquette defined as

$$J_{\rm C}/t = \frac{1}{N_{\rm s}}\sum_{\ell\in{\rm A},\sigma}\sum_{\tau}(-1)^{\tilde{\ell}+\tilde{\tau}}{\rm Im}\langle c^{\dagger}_{\ell+\tau,\sigma}c_{\ell,\sigma} - c^{\dagger}_{\ell,\sigma}c_{\ell+\tau,\sigma}\rangle, \qquad (18)$$

where ℓ runs over all the A sublattice sites, $\tilde{\ell} = \ell_x + \ell_y$, τ indicates the nearest-neighbor directions, and $\tilde{\tau} = 1$ $[-1]$ for $\tau = (\pm1,0)$ $[(0,\pm1)]$. $J_{\rm C}$ is regarded as the order parameter of the SF phase. In the main panel of Fig. 9, we show $|J_{\rm C}|/t$ at half filling as a function of U/t. In the metallic SF phase ($U_{\rm SF} < U < U_{\rm c}$), a relatively large current flows. In the insulating SF phase ($U > U_{\rm c}$), the local current is reduced but still finite. At $U/t = 12$, however, $|J_{\rm C}|/t$ is 1/20 of that in $\Phi_{\rm SF}$ with the same θ. The U/t-dependence of $J_{\rm C}/t$ in this regime is fitted by a curve proportional to $(t/U)^2$ and the system-size dependence is small, as shown in Fig. 9. This suggests that $J_{\rm C}$ in this range of U/t has a localized nature. More specifically, $|J_{\rm c}|$ will be related to the local four-site ring exchange interaction, which appears in the fourth-order perturbation with respect to t/U in the large-U expansion of the Hubbard model.

4. Staggered Flux State at Finite Doping

4.1 *Energy gain and optimized phase parameters*

First, we show the energy gain of $\Psi_{\rm SF}$ with respect to the reference state $\Psi_{\rm N}$ [Eq. (14)] in Fig. 10(a) for four values of the doping rate δ. Similarly to the half-filled case (Fig. 5), ΔE is zero for the weakly correlated regime ($U < U_{\rm SF}$); the value of the SF transition, $U_{\rm SF}/t$, increases as δ increases. The sharp peak of ΔE for $\delta = 0$ changes to a broader peak with a maximum at $U/t \sim 12$ – 16, and finally vanishes at $\delta \equiv \delta_{\rm SF} \sim$

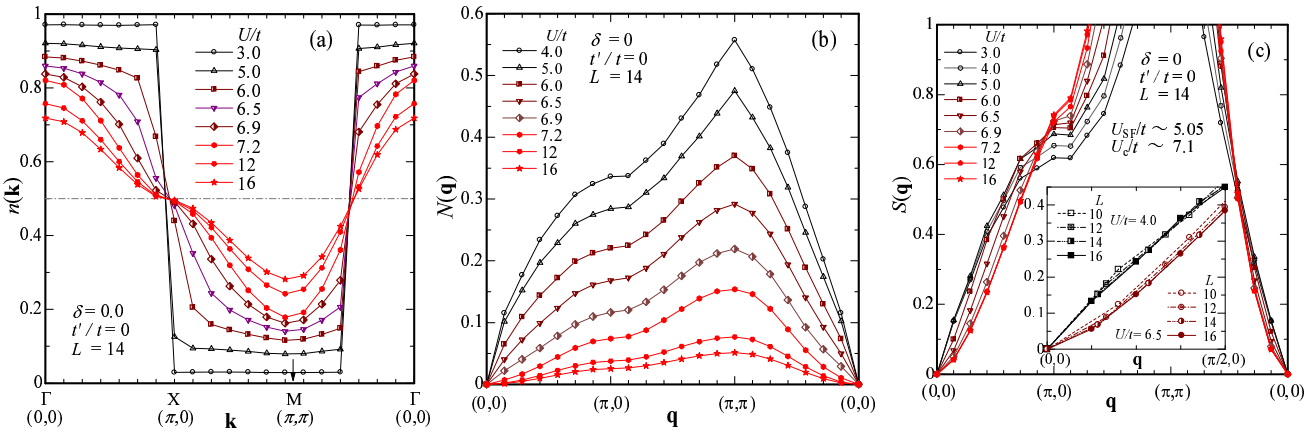

Fig. 8. (Color online) Correlation functions in momentum space of $\Psi_{\rm SF}$ at half filling for various values of U/t. (a) Momentum distribution function, (b) charge density structure factor, and (c) spin structure factor. In the inset in (c), the system-size dependence of $S(\mathbf{q})$ (L = 10–16) for typical cases of a Fermi liquid (U/t = 4) and spin-gap metal (U/t = 6.5) is shown for small $|\mathbf{q}|$ in the direction of $(0,0)$–$(\pi,0)$. See also Ref. 106. Open (black) symbols are for $U < U_{\rm SF}$ (i.e., $\theta = 0$), half-solid (brown) symbols for $U_{\rm SF} < U < U_{\rm c}$, and solid (red) symbols for $U > U_{\rm c}$. For this system size (L = 14), $U_{\rm SF}/t \sim 5.05$ and $U_{\rm c}/t \sim 7.1$.

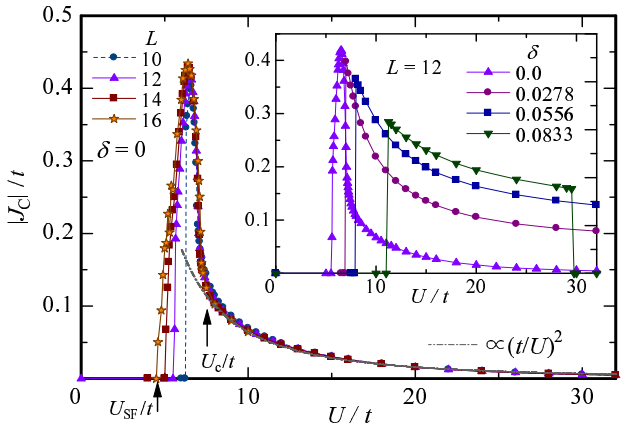

Fig. 9. (Color online) Absolute values of local circular current at half filling as a function of U/t for some system sizes. The SF and Mott transition points are shown by arrows. A curve proportional to $(t/U)^2$ is shown by a gray dash-dotted line. The inset shows the same quantity for some doping rates for L = 12 (discussed in Sect. 4).

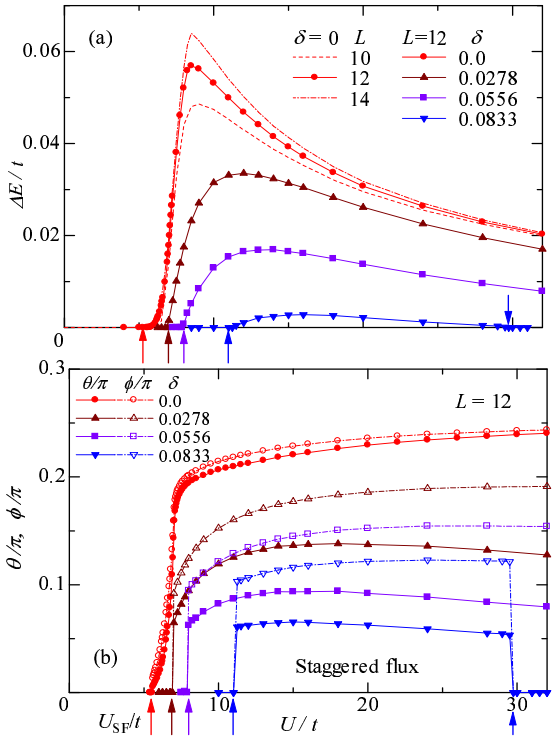

Fig. 10. (Color online) (a) Energy gain of SF state with respect to $\Psi_{\rm N}$ as a function of U/t for four values of doping rate δ (L = 12). For δ = 0, data for three system sizes are shown. (b) Optimized phase parameters θ and ϕ. In both panels, the SF transition is indicated by arrows.

0.1.

In Fig. 10(b), optimized values of the phase parameters are plotted. Both parameters decrease as δ increases. Although θ and ϕ have a discontinuity at $U_{\rm SF}/t$ at this system size, this behavior is owing to a finite-size effect.[107] The SF transition for $L \to \infty$ will be continuous, similarly to the half-filled case. When we compare with the results at $\delta = 0$, we see that $\Phi_{\rm SF}$ is realized in the strongly correlated region ($U > W$), and it is smoothly connected to the Mott insulating state at half filling. It is also interesting that ϕ becomes larger than θ as δ increases, while they are close to each other when $\delta = 0$. This suggests that ϕ overscreens the phase θ in the D-H processes owing to the increasing number of free-holon processes.

Figure 11 shows the δ-dependence of $\Delta E/t$ for the case with U/t = 16. Except for the case with $\delta = 0$, $\Delta E/t$ monotonically decreases as a function of δ. Because the L dependence is appreciable, $\delta_{\rm SF}$ should be somewhat larger in the $L \to \infty$ limit. The behavior of ΔE is consistent with that for the t-J model shown in Appendix B.[108] In the inset of Fig. 11, the δ-dependences of the optimized θ and ϕ are plotted. Their system-size dependences are very small.

4.2 *Various properties*

(i) *Spin-gap metal*: In Fig. 12, we show the behavior of correlation functions in the momentum space $n(\mathbf{k})$, $N(\mathbf{q})$, and $S(\mathbf{q})$ for δ = 0.0556 (L = 12). The U/t-dependences of these quantities are basically similar to those at half filling discussed in Fig. 8. In the region of $U > U_{\rm SF}$, $n(\mathbf{k})$ preserves a discontinuity near $(\pi/2, \pi/2)$, indicating that $\Psi_{\rm SF}$ is always metallic and there is no Mott transition. Furthermore, $N(\mathbf{q})$ is linear in $|\mathbf{q}|$ for $|\mathbf{q}| \to 0$, indicating that the charge degree of freedom is gapless. On the other hand, $S(\mathbf{q})$ appears to be approximately quadratic at small $|\mathbf{q}|$ for $U > U_{\rm SF}$, suggesting that the SF state in the doped region has a gap in the spin

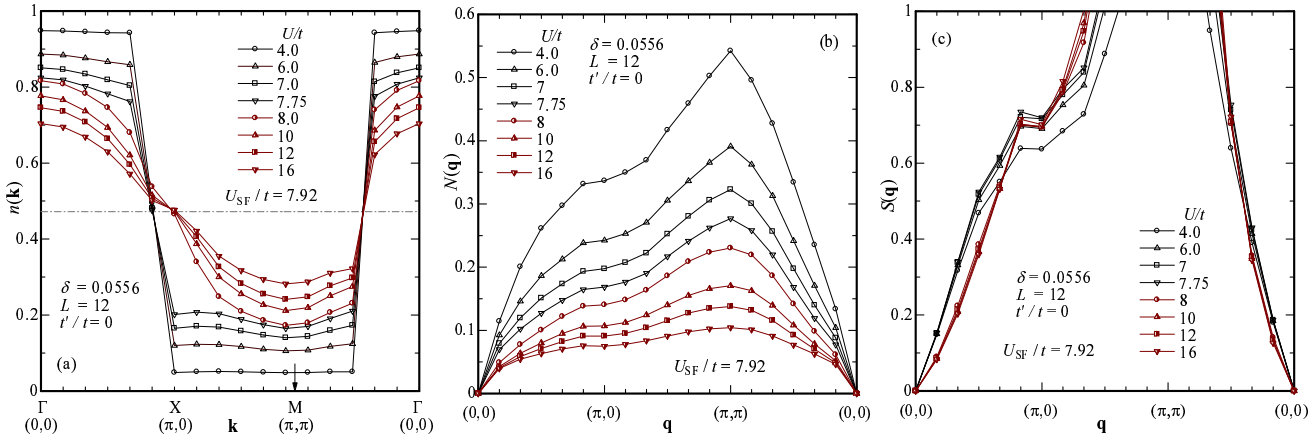

Fig. 12. (Color online) Behavior of (a) momentum distribution function, (b) charge density structure factor, and (c) spin structure factor of Ψ_{SF} for a finite doping ($\delta = 0.0556$) and various values of U/t. Open (black) symbols are for $U < U_{SF}$ and half-solid (brown) symbols are for $U > U_{SF}$. For this system size ($L = 12$) and doping, the SF transition is at $U_{SF}/t = 7.92$.

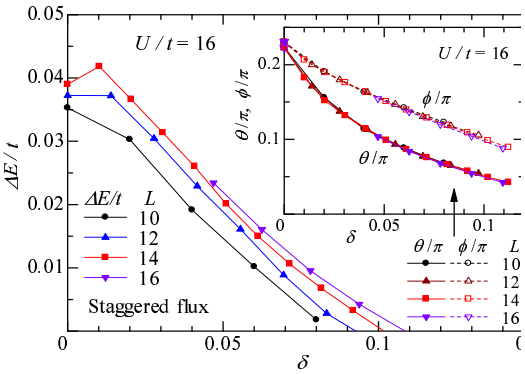

Fig. 11. (Color online) Energy gain of SF state with respect to function of doping rate at $U/t = 16$. Data for four system sizes are the inset, the optimized phase parameters θ and ϕ are shown.

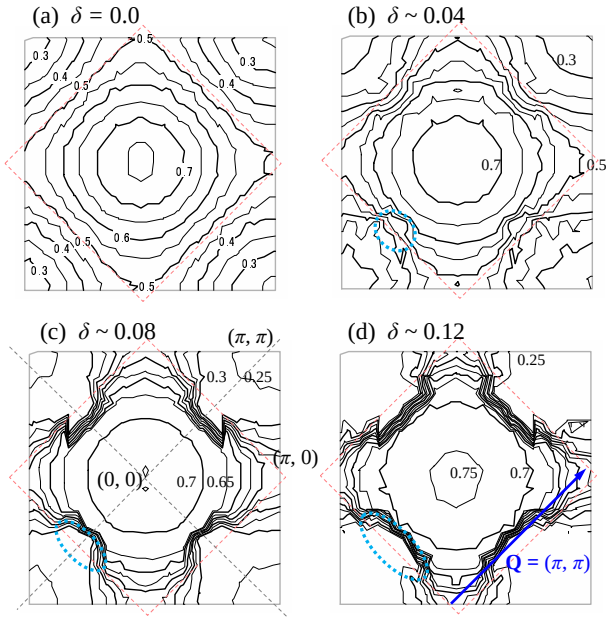

Fig. 13. (Color online) Contour maps of momentum distribution function $n(\mathbf{k})$ of the optimized Ψ_{SF} in the original Brillouin zone for $t'/t = -0.3$, $U/t = 12$, $L = 10 - 14$, and four values of δ in (a)-(d). The wiggles of lines are simply due to the small number of $\mathbf{k}$ points and are not important. The AF Brillouin zone boundary is indicated by pink dotted lines, and zone-diagonal lines are shown with gray dotted lines in (c). Fermi surfaces are indicated with blue ovals in the third quadrants. In (d), the scattering vector of $\mathbf{q} = \mathbf{Q}$ connecting the antinodes, discussed in Sect. 6.4, is shown with a blue arrow.

sector.

(ii) *Segmented Fermi surface*: The bare SF state, Φ_S segmented (or small) Fermi surface around $\mathbf{k} = (\pi/2,$ shown in Appendix A (see Fig. A·4). Here we show t feature is preserved for strongly correlated cases. Sh Fig. 13 are contour maps of $n(\mathbf{k})$ for $U/t = 12$ and four values of δ. Here, we show the data for $t'/t = -0.3$ because Ψ_{SF} is stabilized in a wide doping range (see Fig. 15 later) and the behavior is similar to that for $t'/t = 0$. At half filling, there is no Fermi surface, as shown in panel (a). Upon doping, however, pocket Fermi surfaces appear around $(\pi/2, \pi/2)$ and, as δ increases, they extend to the antinodes along the AF Brillouin zone edge. These Fermi surfaces are shown by blue dashed ovals in panels (b)-(d). A gap remains open near $(\pi, 0)$.

(iii) *Circular currents*: The local circular currents J_C defined in Eq. (18) for the doped cases have already been shown in the inset of Fig. 9, where the evolution of J_C with increasing δ is shown as a function of U/t. We find that J_C increases as δ increases, although the optimized phase parameters θ and ϕ decrease [see Fig. 10(b)]. This is probably because the number of mobile carriers increases as δ increases in the strongly correlated regime, whose feature is typical of a doped Mott insulator. In contrast, as shown in Appendix A, J_C decreases as δ increases in the noninteracting Φ_{SF}. At the phase transition point δ_{SF}, where E(SF) becomes equal to E(N), the or-

maximum value) to zero. This indicates that this transition is first-order, in contrast to the corresponding AF and d-SC transitions, as a function of δ.

5. Effect of Diagonal Hopping t'

In this section, we study the effect of diagonal hopping t' in the two cases shown in Fig. 1.

5.1 *Frustrated square lattice*

Figure 14 summarizes the total energies of Ψ_{SF}, Ψ_N, and Ψ_d as functions of t'/t. Note that the energy for Ψ_N with-

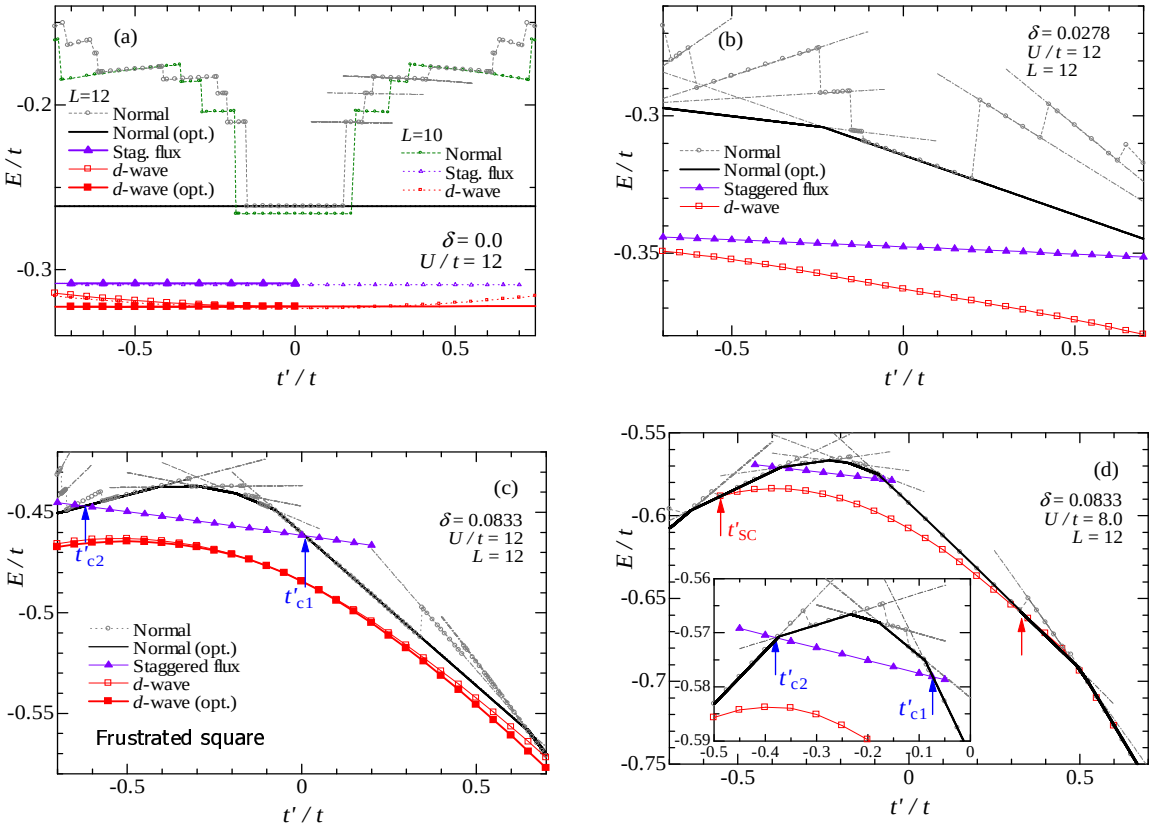

Fig. 14. (Color online) Comparison of total energies among $\Psi_{\rm N}$, $\Psi_{\rm SF}$, and Ψ_d as functions of t'/t in frustrated square lattice of $L = 12$. Panels (a)-(c) display the cases of different doping rates for $U/t = 12$ and (d) shows the case of $U/t = 8$ and $\delta = 0.0833$. In (a), data for $L = 10$ are also shown. Symbols are common to all panels. The black and red bold lines indicate the values of $\Psi_{\rm N}$ and Ψ_d, respectively, when the band-renormalization effect is considered (for details, see Ref. 38). The arrows indicate the positions of the energy crossings. The inset in (d) shows a magnification of the area of energy crossings.

a function of t'/t. This is because the occupied **k**-points in the Fermi surface change discontinuously in $\Phi_{\rm N}$. However, if we consider the band-renormalization effect[38] for $\Psi_{\rm N}$ and use the optimized t_1/t, the lowest energy for $\Psi_{\rm N}$ becomes the black solid line in Fig. 14. We use the solid lines as energies for $\Psi_{\rm N}$. Although we expect some size effects in $\Psi_{\rm N}$, we can see general trends of the energy differences between $\Psi_{\rm SF}$, $\Psi_{\rm N}$, and Ψ_d.

At half filling [Fig. 14(a)], E is symmetric with respect to $t'/t = 0$ owing to the electron-hole symmetry.[35] E(SF) is always lower than E(N) and does not depend on t'/t because $\langle \mathcal{H}_{t'} \rangle = 0$ for any t'/t and U/t. $E(d-{\rm SC})$ tends to increase as $|t'/t|$ increases. (When band renormalization is taken into account, $E(d-{\rm SC})$ also becomes constant.[38,81])

In a slightly doped case [Fig. 14(b)], E for every state becomes a decreasing function of t'/t, but the order of the energies does not change. E(SF) slightly depends on t' and remains a linear function of t'. However, for large δ, the situation changes as shown in Fig. 14(c). The range of E(SF) < E(N) is restricted to $t'_{\rm c2} < t' < t'_{\rm c1}$, as indicated by arrows. This range becomes smaller when U/t decreases [Fig. 14(d)]. We also find that this stable range of $\Psi_{\rm SF}$ becomes smaller as δ increases and finally vanishes at $\delta_{\rm SF} \sim 0.16$ (0.12) for $U/t = 12$ and 16 (8).

Obtaining similar data for different values of δ, t'/t, and L, we construct a phase diagram, as shown in Fig. 15(a). The stable area of the SF state expands above the optimum doping of cuprates ($\delta \sim 0.15$) for $-0.4 \lesssim t'/t \lesssim -0.1$, which corresponds to the hole-doped cuprates. As L increases, the area of $\Psi_{\rm SF}$ tends to expand slightly. For $t'/t > 0$, on the other hand, the area of $\Psi_{\rm SF}$ shrinks to a very close vicinity of half filling, especially for $U/t = 8$.

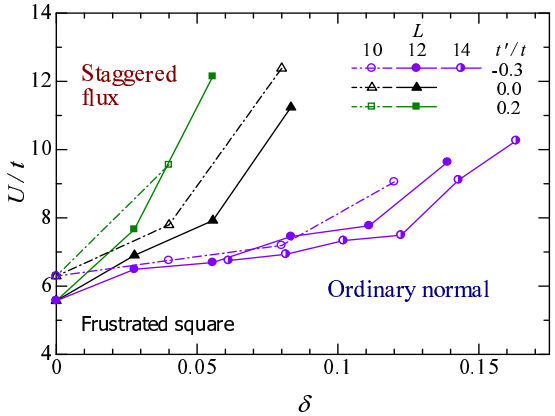

Fig. 16. (Color online) Phase diagram between SF and normal states in δ-U plane for three values of t'/t. The area of the SF phase may be somewhat smaller for $\delta \sim 0$ because the band renormalization in $\Psi_{\rm N}$ is not considered here.

It is useful to draw a phase diagram in the δ-U plane. Figure 16 shows the region in which the SF state is stabilized for the cases with $t'/t = -0.3$, 0, and 0.2. Irrespective of t'/t,

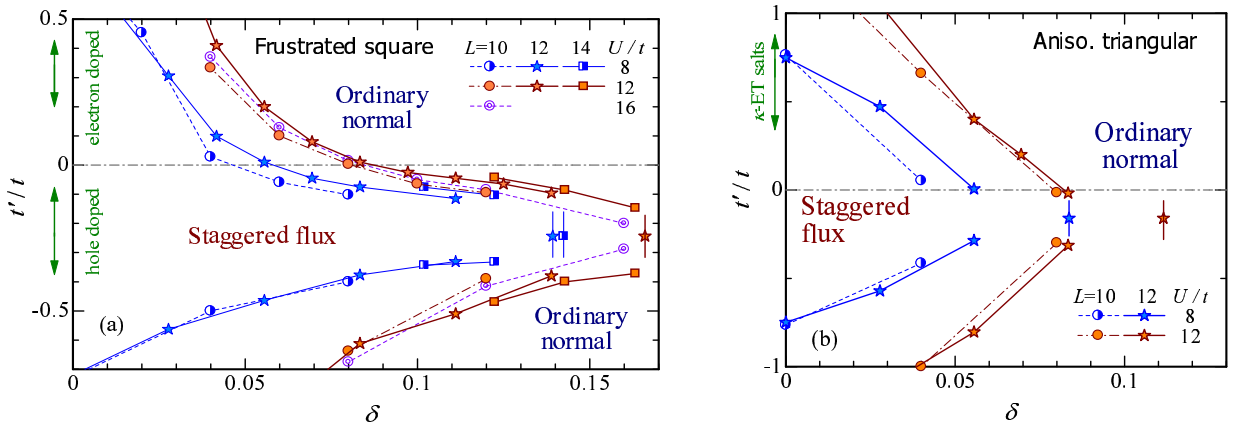

Fig. 15. (Color online) Phase diagrams in the δ-t' plane with doping rate (δ) and frustration strength (t'/t) for (a) the frustrated square lattice and (b) the anisotropic triangular lattice for $U/t = 8$ and 12 [and 16 in (a)]. "Ordinary normal" indicates the projected Fermi sea. The symbols with vertical bars placed at $t'/t \sim -0.25$ indicate that the SF state is not stabilized at these values of δ. The scale of the abscissa is identical in the two panels.

$t'/t = -0.3$ (corresponding to the hole-doped case), the SF is stable in the whole underdoped regime ($\delta \lesssim 0.16$) for $U/t \gtrsim 10$. In contrast, for $t'/t = 0.2$ (electron-doped case), $U_{\rm SF}/t$ rapidly increases as δ increases.

This stability of $\Psi_{\rm SF}$ in a wide range of δ for $-0.4 \lesssim t'/t \lesssim -0.1$ originates primarily from the large t'/t dependence of $\Psi_{\rm N}$ and the very small t'/t dependence of $\Psi_{\rm SF}$. This means that the nature of $\Psi_{\rm SF}$ for $t' = 0$ quantitatively remains that for $t'/t \neq 0$. For example, we show in Fig. 17 the t'/t dependences of the optimized phase parameters and local circular current, $J_{\rm C}$, which do not strongly depend on t'/t. Furthermore, we confirm that the momentum distribution function $n(\mathbf{k})$ is almost the same for $t'/t \neq 0$. Note that this is in sharp contrast to the d-SC state, in which $n(\mathbf{k})$ in the antinodal region markedly changes with t'/t (see Fig. 29 in Ref. 35). The reason for this difference between $\Psi_{\rm SF}$ and Ψ_d will be as follows. Since $\Psi_{\rm SF}$ is very appropriately defined for the simple square lattice, t' change the wave function of $\Psi_{\rm SF}$ only slightly. On the other hand, Ψ_d has a gap opening at the Fermi surface near $(\pi, 0)$, which is markedly affected by t'. In this context, it is natural to expect that extra current, such as diagonal currents in chiral spin states,[111] will not be favored.[83]

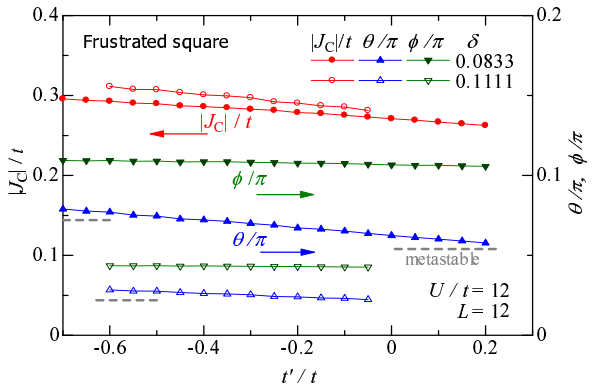

Fig. 17. (Color online) t'/t dependences of the optimized phase parameters θ and ϕ and the local circular current $J_{\rm C}$ in $\Psi_{\rm SF}$ for two values of δ. The unstable regions of $\Psi_{\rm SF}$ are indicated by gray dashed lines and "metastable".

In many studies on the t-J and Hubbard models, the instability toward phase separation has been discussed. Recently, states with AF long-range orders have been shown to be unstable toward phase separation for $t'/t \sim 0$ for the Hubbard model using the VMC method.[35,38,112–114] For the t-J model, an SF state has also been shown to be unstable toward phase separation in a wide range of δ for $t'/t = 0$.[61] Therefore, we need to check this instability in the present case. To this end, we consider the charge compressibility κ or equivalently the charge susceptibility $\chi_{\rm c}$ ($= n^2\kappa$), the inverse of which is given as

$$\chi_{\rm c}^{-1} = \frac{\partial^2 E(n)}{\partial n^2} \sim N_{\rm s}^2 \frac{E(N+4) + E(N-4) - 2E(N)}{4^2}, \quad (19)$$

with $n = N/N_{\rm s}$. If $\chi_{\rm c}^{-1} < 0$, the system is unstable toward phase separation. In Fig. 18, we show the δ dependence of $\chi_{\rm c}^{-1}$ for three values of t'/t and L. We find that $\chi_{\rm c}^{-1}$ is basically negative for $t'/t = 0$ and 0.3, indicating that $\Psi_{\rm SF}$ is unstable toward phase separation (data points of $\delta \sim 0$ should be disregarded because they are affected by the Mott singularity at $\delta \to 0$). This result is consistent with the previous one for the

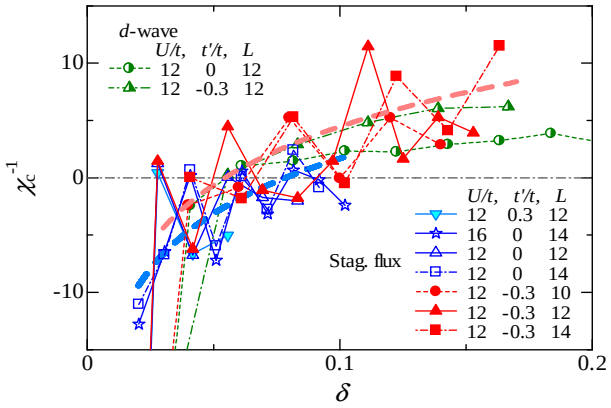

Fig. 18. (Color online) Inverse charge susceptibility of the SF state shown as a function of doping rate δ for some parameter sets for the frustrated square lattice [Fig. 1(a)]. We add guide lines (thick dashed) for $t'/t = 0$ and -0.3 ($U/t = 12$, $L = 14$). The same quantity of the d-SC state is also shown with half-solid green symbols for comparison. Zigzags of the data for $\Psi_{\rm SF}$ are due to the discontinuous change in the occupied $\mathbf{k}$ points and other finite-size effects.

comes positive for $\delta \gtrsim 0.05$ and comparable to that of d-SC (green symbols). Therefore, a homogeneous SF state is possible for the parameters of hole-doped cuprates.

5.2 *Anisotropic triangular lattice*

For the anisotropic triangular lattice, Fig. 19 summarizes the total energies of Ψ_{SF}, Ψ_N, and Ψ_d as a function of t'/t. Again, E(N), the lowest energy of Ψ_N considering band renormalization,[38] is shown by the black solid lines. First, let us consider the half-filled case [Fig. 19(a)]. E is symmetric with respect to $t'/t = 0$ owing to the electron-hole symmetry.[35] Similarly to the case on the frustrated square lattice, E(FS) and E(d−SC) (if the band renormalization is considered[115,116]) are constant. For the ground state, we find from Fig. 19(a) that Ψ_N has a lower energy than Ψ_d for $t' > t'_{SC}$ with $t'_{SC}/t = 0.807$ for $L = 12$. However, the (π,π)-AF state or incommensurate AF states including the case of a 120° structure has a lower energy at half filling.[115–117]

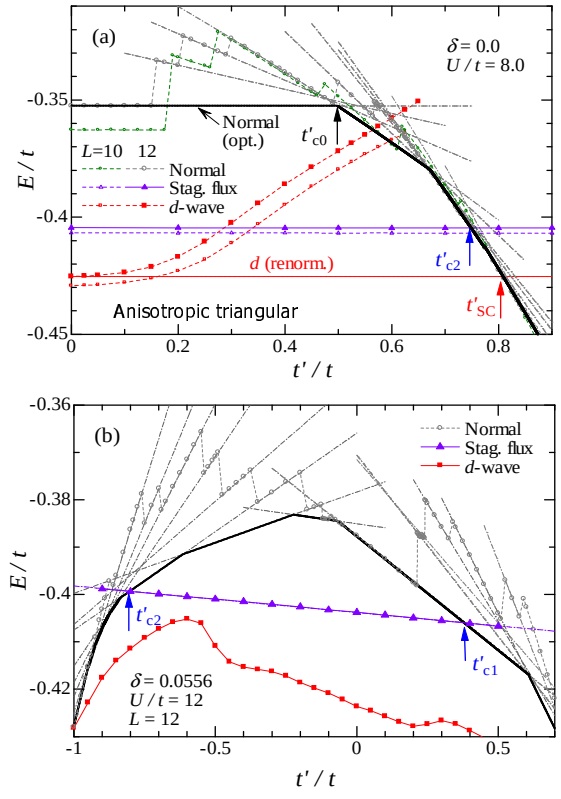

Fig. 19. (Color online) Comparison of total energy among Ψ_N, Ψ_{SF}, and Ψ_d as functions of t'/t. Panel (a) displays the half-filled case for $U/t = 8$ (only the data for $t'/t \geq 0$ are shown) and $L = 10$ and 12, and (b) a doped case for $U/t = 12$ ($\delta = 0.0556$) and $L = 12$. We show the optimized values by the band renormalization for Ψ_N with (black) solid lines. The band-renormalized data for Ψ_d are also shown in (a) with a (red) solid line.

We compare the energies between Ψ_N and Ψ_{SF}, assuming that AF states are not stabilized. In Fig. 19(a), Ψ_{SF} is more stable than Ψ_N for $t' < t'_{c2}$ with $t'_{c2}/t = 0.749$ (0.763) for $U/t = 8$ and $L = 12$ (10). We employ the value $U/t = 8$ simply because it is frequently used as a plausible value for κ-ET salts.[73] Actually, Ψ_{SF} is Mott insulating at $U/t = 8$; a value of $U/t \lesssim 7.1$ is necessary for a metallic state. However, the point is insulating or metallic. On the basis of similar calculations for various values of U/t and t'/t, we construct a phase diagram within the SF and normal state at half filling (Fig. 20), which is relevant for organic conductors. The boundary value U_{SF}/t between Ψ_{SF} and Ψ_N increases as t'/t increases.

As shown before, the Mott transition occurs at $U_c \sim 7.1t$ for $t' = 0$. Since the properties of Ψ_{SF} are similar to the case of $t' = 0$, the SF state is metallic for $U \lesssim U_c$ and insulating for $U > U_c$. This phase boundary is also shown in Fig. 20.

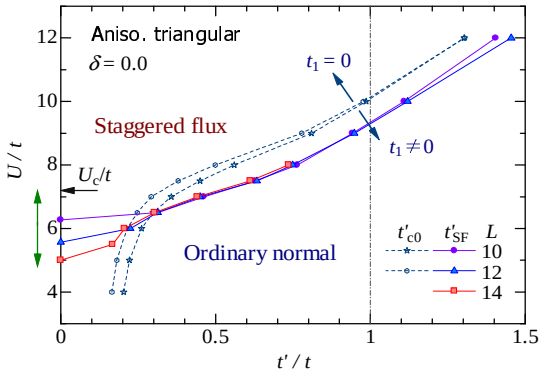

Fig. 20. (Color online) Phase diagram between the SF and normal states in t'-U plane at half filling on anisotropic triangular lattice. Boundaries (U_{SF}, solid lines) are determined for three system sizes. The green arrow near the vertical axis represents the range of the metallic SF state. The dashed lines show the boundary in Ψ_N regarding whether the nesting condition is restored ($t_1 = 0$) or not ($t_1 \neq 0$) in the renormalized band (see Sect. 6.2 later).

For a doped case, we show in Fig. 19(b) the t'/t dependence of the total energy for the three states for typical parameters. It is noteworthy that E/t for Ψ_N and Ψ_d decreases rapidly for large values of $|t'/t|$ (~ 1). Obtaining similar data for various values of t'/t and δ, we construct a phase diagram in the δ-t' space [Fig. 15(b)]. Compared with the case of the frustrated square lattice [Fig. 15(a)], the area of Ψ_{SF} is restricted to the small doping region.

6. Discussion

6.1 *Phase cancelation mechanism*

First, let us consider intuitively why Ψ_{SF} has a low energy in the strongly correlated region of the Hubbard model. As discussed in a previous study,[35] the processes corresponding to the J term in the t-J model are those in which a D-H pair is created or annihilated as shown in Fig. 21(a). Generally speaking, the phase yielded in this process causes a loss of kinetic energy. In order to reduce this kinetic energy loss, the phase θ should be eliminated by the phase ϕ by applying $\mathcal{P}_\theta$ with $\phi \sim \theta$ in the same manner as introduced in Ref. 72.

We expect a similar phenomenon in the Heisenberg interaction in the t-J model. In the J term, an ↑ spin at site i hops to site j ($= i+\tau$) and simultaneously a ↓ spin at site j hops to site i. As shown in Fig. 21(b), if the former hopping yields a phase θ, the latter yields $-\theta$ in Φ_{SF}; the total phase in the exchange process precisely cancels out (shown in the square brackets in Fig. 21). Since the two processes occur simultaneously, it is unnecessary to introduce ϕ in the t-J model to stabilize the SF state. On the other hand, in the Hubbard model [Fig. 21(a)],

sarily occur immediately after a D-H pair is created; these two processes are mutually independent events. Therefore, it is necessary to introduce the phase ϕ to eliminate $\pm\theta$ in each process in order to stabilize the SF state.

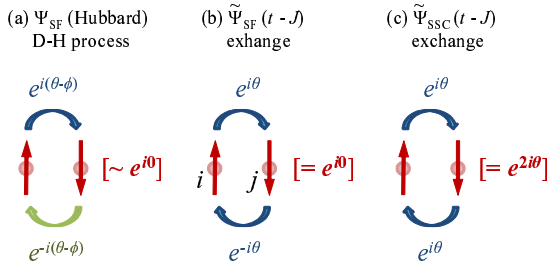

Fig. 21. (Color online) Illustration of phase factors added in (a) creation or annihilation process of doublon-holon (D-H) pair in Ψ_{SF} for large-U/t Hubbard model, (b) spin exchange process in $\tilde{\Psi}_{SF}$ for t-J model, and (c) spin exchange process in $\tilde{\Psi}_{SSC}$ for t-J model. For details, see text.

Finally, let us apply the present mechanism to the spin-current-carrying state. Staggered spin current (SSC) states (or sometimes called spin-nematic states[63]) have been considered to be candidates for hidden orders in various systems.[118] In these states, counter-rotating currents of $\uparrow$ and $\downarrow$ spins alternately flow in each plaquette [Fig. A·1(b)]. We have carried out similar VMC calculations for the projected SSC state $\tilde{\Psi}_{SSC} = \mathcal{P}_G(0)\Phi_{SSC}$. The results are summarized in Appendix C. We conclude that $\tilde{\Psi}_{SSC}$ is not stabilized for any J/t and underdoped δ. We can easily see the reason for this by considering the phase cancelation. As we can see from Fig. 21(c), the total phase added in an exchange process in $\tilde{\Psi}_{SSC}$ remains 2θ. We found that this phase is difficult to eliminate by configuration-dependent phase factors such as $\mathcal{P}_\phi$. Therefore, we conclude that the SSC state or spin-nematic state will never be stabilized.

6.2 *Kinetic energy gain*

We discuss another physical reason for the stabilization of the SF state. In Fig. 22. we show the difference in the kinetic energy ΔE_t and interaction energy ΔE_U between the optimal SF state and the projected Fermi sea,

$$\begin{aligned} \Delta E_t &= E_t(\mathrm{N}) - E_t(\mathrm{SF}), \\ \Delta E_U &= E_U(\mathrm{N}) - E_U(\mathrm{SF}), \end{aligned} \tag{20}$$

for four values of δ. In previous papers, we perfomed the same analysis for Ψ_d and Ψ_N,[33,34] and showed that the SC transition is driven by the kinetic energy gain for $U \gtrsim U_{co}$ with U_{co}/t being the crossover value from weakly to strongly correlated regimes. In Fig. 22, we find that a similar phenomenon emerges between Ψ_{SF} and Ψ_N: Kinetic energy gain occurs in the strongly correlated region. The physical reason for this will be as follows. In the strongly correlated regime, the kinetic energy is dominated by the D-H pair creation or annihilation processes (not shown). Since the phases arising in these processes are canceled out by ϕ, this kinetic energy gain corresponds to that in the J-term in the t-J model.

In Fig. 23. we show a similar comparison between the d-SC and optimal SF states, i.e.,

$$\Delta E_U = E_U(\mathrm{SF}) - E_U(d\text{–}\mathrm{SC}). \tag{21}$$

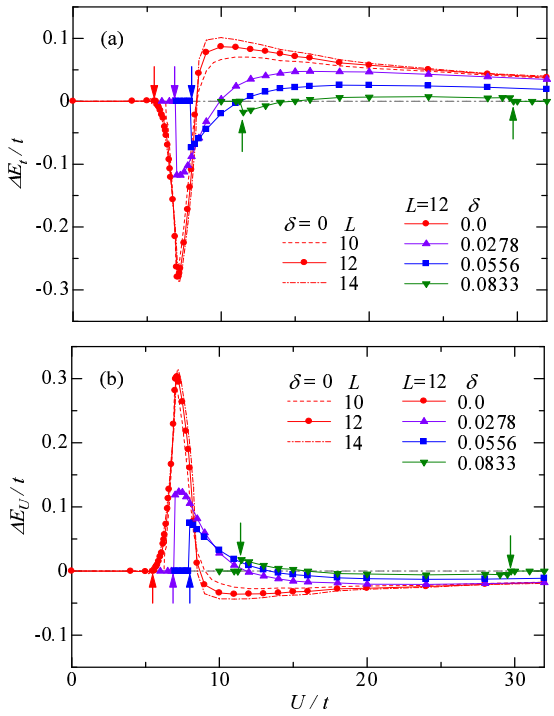

Fig. 22. (Color online) The two components of the energy difference between the SF state and the projected Fermi sea are shown for some doping rates ($t'/t = 0$, $U/t = 12$): (a) kinetic energy and (b) interaction energy parts. For $\delta = 0$, we add data for $L = 10$ and 14. The arrows indicate U_{SF}/t for $L = 12$.

In particular, in the regime of $U > U_c(\mathrm{SF})$ at half filling and $U > U_{SF}$ for $\delta > 0$, the energy gain occurs exclusively in the kinetic part ($\Delta E_t > 0$ and $\Delta E_U < 0$). Thus, the cause of stabilization both in $\Psi_N \to \Psi_{SF}$ and in $\Psi_{SF} \to \Psi_d$ is the kinetic energy gain for a sufficiently large U/t.[119]

6.3 *Comparison with experiments*

(i) *High-T_c cuprates*: Here, we discuss the lattice translational symmetry, which is broken in the present SF state. The peaks arising from local loop currents in the polarized neutron scattering spectra are found at $\mathbf{k} = (0,0)$,[17–19] suggesting that the lattice translational symmetry is preserved in the pseudogap phase. Some authors have argued that the SF state breaks this symmetry, but physical quantities calculated with SF states display a $(0,0)$ peak in addition to a (π,π) peak.[120] The above neutron experiments appear to be consistent with more complicated circular-current states that do not break this symmetry.[90,121,122] Recently, however, one of the authors showed that this type of circular-current state is not stabilized with respect to the normal state in a wide range of the model parameters on the basis of systematic VMC calculations with refined wave functions for d-p-type models. Instead, SF states are stabilized in some parameter ranges.[123] On the other hand, the shadow bands observed in the ARPES spectra,[24–27] which also characterize the pseudogap phase, seem to require the scattering of (π,π) and a folded Brillouin zone. Therefore, the issue of translational symmetry breaking is still controversial.

(ii) *Organic conductors*: In Sect. 5.2, we studied the anisotropic triangular lattice. Let us here discuss the relevance of the present results to experiments. As discussed in

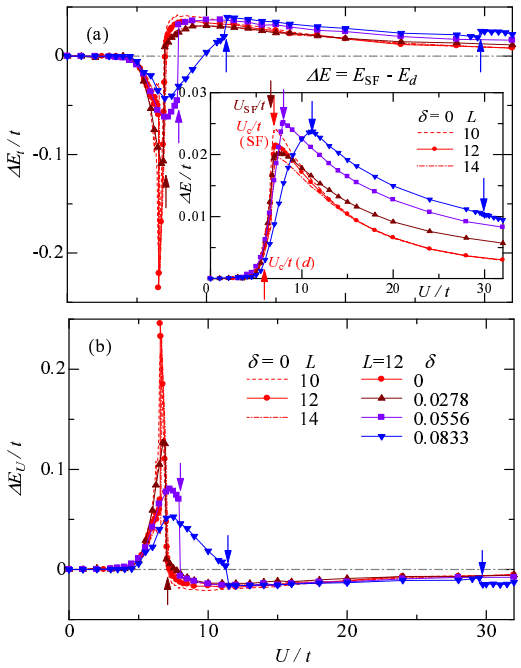

Fig. 23. (Color online) The two components of the energy difference between the d-SC and SF states are shown for some doping rates ($t'/t = 0$, $L = 12$): (a) kinetic energy and (b) interaction energy parts. The symbols are common to all panels. For $\delta = 0$, data for $L = 10$ and 14 are added. The arrows indicate U_{SF}/t in the SF state for $\delta > 0$. The inset in (a) shows the difference in total energy ($\Delta E = \Delta E_t + \Delta E_U$) for four values of δ.

The present results show that the SF state is stabilized for the case of $t'/t \sim 0.4$. Therefore, the pseudogap behavior for $T > T_c$ observed in deuterated κ-$(ET)_2Cu[N(CN)_2]Br$ is probably caused by the SF state. On the other hand, κ-$(ET)_2Cu_2(CN)_3$ with $t'/t \sim 0.8$ shows Fermi-liquid-like behavior above T_c. Since the present result shows that the SF state is not stabilized for the case of $t'/t \sim 0.8$, the normal state of κ-$(ET)_2Cu_2(CN)_3$ is naturally understood on the basis of Ψ_N. Although our results are consistent with experiments, quantitative discussions will be necessary to determine the effective value of U/t as well as t'/t more accurately for each compound..[124,125]

For the organic conductors with finite doping, we find that Ψ_{SF} is not stabilized at $\delta = 0.11$ for both $U/t = 8$ and 12, regardless of the value of t'/t. Thus, concerning the pseudogap phenomena found in a doped κ-ET salt,[79] we cannot conclude that the SF state is a candidate for the pseudogap phase. Other factors may be necessary to understand this pseudogap.

6.4 Related studies and coexistence with other orders

A decade ago, Yang, Rice, and Zhang introduced a phenomenological Green's function that can represent various anomalous properties of the pseudogap phase.[126] Their Green's function contains a self-energy that reproduces the $d_{x^2-y^2}$-wave RVB state at half filling. For finite doping, the Green's function is assumed to have the same self-energy but without the features of SC. On the other hand, the SF state used in the present paper is also connected to the $d_{x^2-y^2}$-wave RVB state due to the SU(2) symmetry at half filling. For finite doping, however, the SF state does not show SC. Therefore, we expect a close relationship between the present SF state and the phenomenological Green's function, although the explicit correspondence is not known.

As mentioned in Sect. 1, an AF state was recently studied by applying a VMC method with a band-renormalization effect to the Hubbard model on the frustrated square lattice.[38] It revealed that the AF state is considerably stable and occupies a wide range of the ground-state phase diagram. In doped metallic cases for $t'/t \lesssim -0.05$, an AF state called type-(ii) AF state is stabilized, while for $t'/t \gtrsim -0.05$, a type-(i) AF state is stabilized. In a type-(ii) AF state, a pocket Fermi surface arises around $(\pi/2, \pi/2)$ and a gap opens in the antinode [near $(\pi, 0)$]. As δ increases, the Fermi surface around $(\pi/2, \pi/2)$ extends toward the antinodes along the AF Brillouin zone edge. Such behavior resembles the pseudogap phenomena, as the SF state treated in this paper does. Thus, if such features are preserved when the AF long-range order is broken into a short-range order for some reason, as actually observed in cuprates,[127] a (disordered) type-(ii) AF state becomes another candidate for a pseudogap state, although the symmetry breaking is rather different from that in the SF state.

Let us discuss the coexistence with d-SC. The same study[38] as discussed above showed that, although type-(ii) AF states do not coexist with d-SC, metallic AF states for $t'/t \gtrsim -0.05$ [called type-(i) AF] coexist with d-SC; these type-(i) AF states have pocket Fermi surfaces in the antinodes. This corroborates the fact that the electron scattering of $\mathbf{q} = (\pi, \pi)$ that connects two antinodes is crucial for the appearance of d-SC. From this result, we expect that the SF state is unlikely to coexist with d-SC because gaps open in the antinodes in the SF state, as shown in Fig. 13(d). As an exception, coexistence may be possible for $\delta \sim \delta_{SF}$, where the Fermi surfaces extend to the antinodes, as discussed in Ref. 38. Thus, the SF order probably competes with the d-SC order rather than underlies it.[128] We need to directly confirm this by examining a mixed state of the SF and d-SC orders.

Finally, we consider the possibility of the coexistence of AF and SF orders. Recently, a Hubbard model with an SF phase, namely, $\mathcal{H} = \mathcal{H}^{SF} + \mathcal{H}_U$ [see Eqs. (1) and (A·1)], was studied using a VMC method with a mixed state of SF and AF orders, Ψ_{SF+AF}.[129] For $\theta = 0$ [Eq. (1) with $t' = 0$], the optimized Ψ_{SF+AF} is reduced to Ψ_{AF}, which belongs to the type-(i) AF phase. Namely, the SF order is excluded by the type-(i) AF order. This is probably because the AF order is energetically dominant over the SF order, and the loci of Fermi surfaces compete with each other.

7. Conclusions

In this paper, we studied the stability and other properties of the staggered flux (SF) state in the two-dimensional Hubbard model at and near half filling. We carried out systematic computations for U/t, t'/t, and δ, using a variational Monte Carlo method, which is useful for treating correlated systems. In the trial SF state, a configuration-dependent phase factor was introduced, which is vital to treat a current-carrying state in the regime of Mott physics. In this SF state, we found a good possibility of explaining the pseudogap phenomena in high-T_c cuprates and κ-ET salts. The main results are summarized as follows:

(1) The SF state is not stabilized in a weakly correlated regime ($U/t \lesssim 5$), but becomes considerably stable in a strongly correlated regime [Figs. 5 and 10(a)]. The physical

t-J model.[32,43,44,60] The transition from $\Psi_{\rm N}$ to $\Psi_{\rm SF}$ at $U_{\rm SF}/t$ is probably continuous.

(2) At half filling ($\delta = 0$), the SF state becomes Mott insulating for $U > U_{\rm c} \sim 7t$. A metallic SF state is realized for $U_{\rm SF} < U < U_{\rm c}$, which is gapless in the charge degree of freedom but gapped in the spin sector. This gap behavior of the metallic SF state at $\delta = 0$ continues to the doped cases of $U > U_{\rm SF}$. However, it is distinct from the case of the noninteracting SF state $\Phi_{\rm SF}$ in the sense that spin-charge separation occurs. In doped cases, $\Psi_{\rm SF}$ has a segmentary Fermi surface near the nodal point $(\pi/2, \pi/2)$ but is gapped near the antinodal $(\pi, 0)$ (Fig. 13). By analyzing the kinetic energies (E_t), we found that $E_t(\Psi_d) < E_t(\Psi_{\rm SF}) < E_t(\Psi_{\rm N})$ for a large U/t, meaning that a kinetic-energy-driven SC takes place even if we assume that the SF state is realized above $T_{\rm c}$.

(3) Although $\Psi_{\rm SF}$ is unstable toward phase separation for $t'/t \sim 0$ in accordance with the feature in the t-J model,[61] $\Psi_{\rm SF}$ restores stability against inhomogeneity for $t'/t \sim -0.3$. This aspect is similar to that of AF states.[35,38,113]

(4) For the simple square lattice ($t'/t = 0$), the stable SF area is $\delta \lesssim 0.1$. In the anisotropic triangular lattice ($|t'/t| > 0$), this area does not expand. In the frustrated square lattice, however, the t' term makes this area expand to $\delta \lesssim 0.16$ for $-0.4 \lesssim t'/t \lesssim -0.1$ (hole-doped cases) but shrink to a very close vicinity of half filling for $t'/t > 0$ (electron-doped cases) (Fig. 15). This change is mostly caused by the sensitivity of $\Psi_{\rm N}$ to t', while $\Psi_{\rm SF}$ is insensitive to t' because it is defined suitably for the square-lattice plaquettes. This result may be related to the fact that pseudogap behavior is not clearly observed in electron-doped cuprates.[130–135]

(5) On the basis of this study and another study,[38] we argue that the SF state does not coexist with d-SC as a homogeneous state and is not an underlying normal state from which d-SC arises. This is because the SF state has no Fermi surface in the antinodes necessary for generating d-SC. However, when the optimized θ becomes small (for $\delta \sim \delta_{\rm SF}$), coexistence is possible. The coexistence of SF and AF orders also does not occur for $t'/t \gtrsim -0.05$;[129] further study is needed to clarify the cases of $t'/t \lesssim -0.05$.

(6) The local circular current in a plaquette, which is an order parameter of the SF phase, is strongly suppressed in the large-U/t region, but it does not vanish even in the insulating phase. A so-called chiral Mott insulator is realized.

(7) We showed that the spin current state (or spin-nematic state) is not stabilized for the t-J and Hubbard models.

Because these results are mostly consistent with the behaviors in the pseudogap phase of cuprates, the SF state should be reconsidered as a candidate for the anomalous 'normal state' competing with d-SC in the underdoped regime. Note that the AF state is considerably stabilized in a wide region of the Hubbard model.[38] Therefore, possible disordered AF [type-(ii)] is another candidate for the pseudogap phase, although the symmetry breaking is different. Besides this claim, there are relevant subjects left for future studies. (i) What will be the phase transition between the SF and d-SC states if the SF state is the state above $T_{\rm c}$? (ii) In this study, we treated the SF and d-SC states independently. However, it is important to check directly whether the two orders coexist,[15,28,29] and how the coexistent state behaves, if it exists.[44,136] (iii) In this study, we introduced a phase factor for the doublon-holon processes. It will be a subject to search for a low-lying circular-current state other than the SF state and the state proposed by Varma.[90,121,122]

We thank Yuta Toga, Ryo Sato, Tsutomu Watanabe, Hiroki Tsuchiura, and Yukio Tanaka for useful discussions and information. This work was supported in part by Grants-in-Aid from the Ministry of Education, Culture, Sports, Science and Technology.

Appendix A: Details of Bare Staggered Flux State

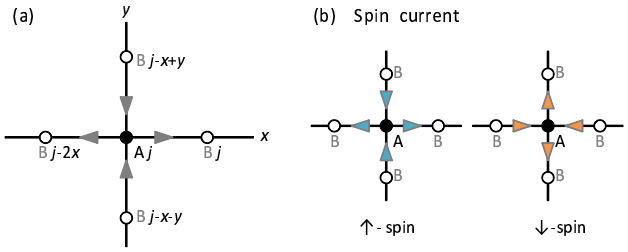

Fig. A·1. (Color online) (a) Coordinates in the extended unit cell used in $\mathcal{H}_{\rm SF}$. (b) Currents in staggered spin current state for up and down spins discussed in Appendix C. The arrows denote the directions of easy flow.

In this Appendix, we give a definition of the one-body SF state $\Phi_{\rm SF}$ used in this study (see Sect. 2.2) and summarize its characteristic properties. $\Phi_{\rm SF}$ is the ground state of a noninteracting SF Hamiltonian $\mathcal{H}^{\rm SF}(\theta)$ written as

$$\mathcal{H}^{\rm SF} = -t \sum_{j\in A,\sigma} \Big[e^{i\theta} \left(c^{\dagger}_{{\rm A}j,\sigma} c_{{\rm B}j,\sigma} + c^{\dagger}_{{\rm A}j,\sigma} c_{{\rm B}j-2\mathbf{x},\sigma} \right) + e^{-i\theta} \left(c^{\dagger}_{{\rm A}j,\sigma} c_{{\rm B}j-\mathbf{x}+\mathbf{y},\sigma} + c^{\dagger}_{{\rm A}j,\sigma} c_{{\rm B}j-\mathbf{x}-\mathbf{y},\sigma} \right) + {\rm H.c.} \Big] \qquad (A\cdot1)$$

in the sublattice (A,B) representation [see Fig. A·1(a)]. Here, we abbreviate $\mathbf{r}_j$ (the position of site j) as j, and $\mathbf{x}$ ($\mathbf{y}$) is the unit vector in the x (y) direction. For $\theta = 0$, $\mathcal{H}^{\rm SF}$ is reduced to $\mathcal{H}_t$ in Eq. (1). $\mathcal{H}^{\rm SF}$ is diagonalized as

$$\mathcal{H}^{\rm SF} = \sum_{\mathbf{k},\sigma} \left[E^{\rm SF}_{-}(\mathbf{k})\, \alpha^{\dagger}_{\mathbf{k}\sigma} \alpha_{\mathbf{k}\sigma} + E^{\rm SF}_{+}(\mathbf{k})\, \beta^{\dagger}_{\mathbf{k}\sigma} \beta_{\mathbf{k}\sigma} \right], \qquad (A\cdot2)$$

with the band dispersions given as

$$E^{\rm SF}_{\pm}(\mathbf{k}) = \pm 2t\, \mathcal{S}_{\theta,\mathbf{k}}, \qquad (A\cdot3)$$

by applying the unitary transformation

$$\begin{pmatrix} c_{{\rm A}\mathbf{k}\sigma} \\ c_{{\rm B}\mathbf{k}\sigma} \end{pmatrix} = \frac{1}{\sqrt{2}} \begin{pmatrix} \gamma_{\theta,\mathbf{k}} & \gamma_{\theta,\mathbf{k}} \\ 1 & -1 \end{pmatrix} \begin{pmatrix} \alpha_{\mathbf{k}\sigma} \\ \beta_{\mathbf{k}\sigma} \end{pmatrix}, \qquad (A\cdot4)$$

where

$$\gamma_{\theta,\mathbf{k}} = \frac{e^{-ik_x} \left(e^{i\theta} \cos k_x + e^{-i\theta} \cos k_y \right)}{\mathcal{S}_{\theta,\mathbf{k}}} \qquad (A\cdot5)$$

with $\mathcal{S}_{\theta,\mathbf{k}}$ given in Eq. (6). The lower band dispersion can be transformed to the form of Eq. (7). The one-body SF state for $n \le 1$ is given by filling the lower band as

$$\Phi_{\rm SF} = \prod_{\mathbf{k}\in\mathbf{k}_{\rm F}(\theta),\sigma} \alpha^{\dagger}_{\mathbf{k}\sigma} |0\rangle = \prod_{\mathbf{k}\in\mathbf{k}_{\rm F}(\theta),\sigma} \frac{1}{\sqrt{2}} \left(\gamma_{\theta,\mathbf{k}}\, c^{\dagger}_{A\mathbf{k}\sigma} + c^{\dagger}_{B\mathbf{k}\sigma} \right) |0\rangle, \qquad (A\cdot6)$$

which leads to Eq. (4) by applying the Fourier transformation,

$$c_{\Lambda j\sigma} = \sqrt{\frac{2}{N}} \sum_{\mathbf{k}} e^{i\mathbf{k}\cdot\mathbf{r}_j} c_{\Lambda\mathbf{k}\sigma}. \qquad (\Lambda = {\rm A}, {\rm B}) \qquad (A\cdot7)$$

Because $\Phi_{\rm SF}$ is a current-carrying state, $\Phi_{\rm SF}$ is essentially complex except when $4\theta = 0$ and π.

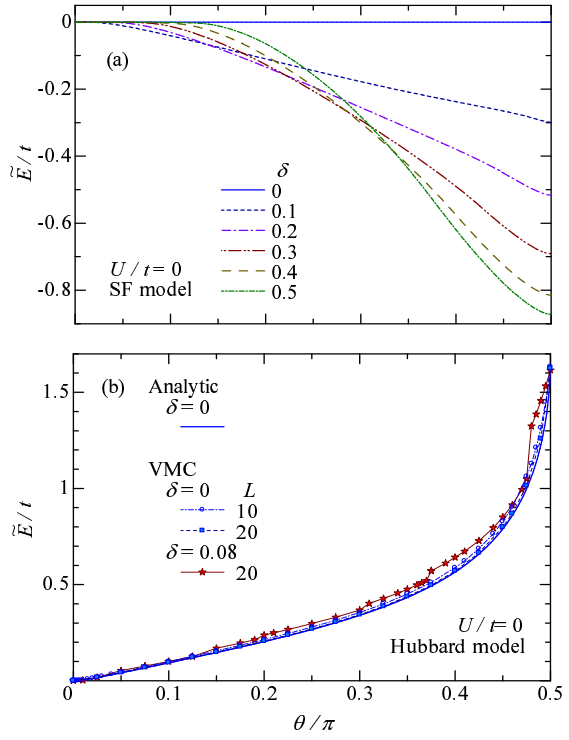

Fig. A·2. (Color online) Total energies per site of $\Phi_{\rm SF}$ measured from that of $\Phi_{\rm N}$ [Eq. (A·8)] are drawn as functions of θ for (a) the SF Hamiltonian [Eq. (A·1)] and (b) the Hubbard Hamiltonian [Eq. (1)]. In (a), Eqs. (A·10) and (A·12) are used with a common θ in $\Phi_{\rm SF}$ and $\mathcal{H}^{\rm SF}$ as the ground state. In (b), Eqs. (A·9) and (A·11) are used with θ being varied in $\Phi_{\rm SF}$; we plot VMC data for some cases in addition to the analytic result at half filling. We confirmed that $\mathcal{P}$ has almost no effect for $U = 0$. t' is fixed at 0.

The total energy per site of $\Phi_{\rm SF}$ measured from that of the bare Fermi sea $\Phi_{\rm N}$ is written as

$$\tilde{E} = E_{\rm SF} - E_{\rm N}. \tag{A·8}$$

Here, $E_{\rm N}$ for $\Psi_{\rm N}$ is obtained for the Hubbard model [Eq. (1) with $U = 0$] through

$$E_{\rm N} = \frac{1}{N_{\rm s}} \frac{\langle \Phi_{\rm N}|\mathcal{H}_t|\Phi_{\rm N}\rangle}{\langle \Phi_{\rm N}|\Phi_{\rm N}\rangle} = \frac{1}{N_{\rm s}} \sum_{\mathbf{k}\in\mathbf{k}_{\rm F}(\theta=0),\sigma} \varepsilon_{\mathbf{k}}, \tag{A·9}$$

where $\varepsilon_{\mathbf{k}}$ [Eq. (8)] is the bare dispersion of an ordinary Fermi sea, and $E_{\rm N}$ is obtained for the SF model [Eq. (A·1)] through

$$E_{\rm N} = \frac{1}{N_{\rm s}} \frac{\langle \Phi_{\rm N}|\mathcal{H}^{\rm SF}|\Phi_{\rm N}\rangle}{\langle \Phi_{\rm N}|\Phi_{\rm N}\rangle} = \frac{1}{N_{\rm s}} \sum_{\mathbf{k}\in\mathbf{k}_{\rm F}(\theta=0),\sigma} E_-^{\rm SF}(\mathbf{k}). \tag{A·10}$$

The energy of $\Phi_{\rm SF}$ for the Hubbard model is given by

$$E_{\rm SF} = \frac{\langle \Phi_{\rm SF}|\mathcal{H}_t|\Phi_{\rm SF}\rangle}{N_{\rm s}\langle \Phi_{\rm SF}|\Phi_{\rm SF}\rangle} = -\frac{2t\cos\theta}{N_{\rm s}} \sum_{\mathbf{k}\in\mathbf{k}_{\rm F}(\theta),\sigma} \frac{\left(\cos k_x + \cos k_y\right)^2}{\mathcal{S}_{\theta,\mathbf{k}}}, \tag{A·11}$$

and that for the SF Hamiltonian is given by

$$E_{\rm SF} = \frac{1}{N_{\rm s}} \frac{\langle \Phi_{\rm SF}|\mathcal{H}^{\rm SF}|\Phi_{\rm SF}\rangle}{\langle \Phi_{\rm SF}|\Phi_{\rm SF}\rangle} = \frac{1}{N_{\rm s}} \sum_{\mathbf{k}\in\mathbf{k}_{\rm F}(\theta),\sigma} E_-^{\rm SF}(\mathbf{k}). \tag{A·12}$$

In Fig. A·2(a), we show $\tilde{E}/t$ for $\mathcal{H}^{\rm SF}$ as a function of θ. Be-

half filling, $E_{\rm SF}$ and $E_{\rm N}$ are identical because the Fermi surfaces of $\Phi_{\rm N}$ and $\Phi_{\rm SF}$ are identical, but the energy of $\Phi_{\rm SF}$ is sizably reduced as δ or θ increases. In contrast, for the Hubbard model with $U = 0$ ($\mathcal{H}_t$), $\tilde{E}/t$ is positive because the exact ground state of $\mathcal{H}_t$ is $\Phi_{\rm N}$ [$\Phi_{\rm SF}(\theta = 0)$]. $\tilde{E}/t$ monotonically increases as θ increases, as shown in Fig. A·2(b). For $\theta \sim 0$, $E_{\rm SF}$ in Eq. (A·11) increases quadratically as

$$E_{\rm SF} = E_{\rm N} + \theta^2 t \sum_{\mathbf{k}\in\mathbf{k}_{\rm F}(\theta),\sigma} \frac{\left(\cos k_x - \cos k_y\right)^2}{\left|\cos k_x + \cos k_y\right|} + \cdots, \tag{A·13}$$

at least for $\delta = 0$. Hence, the SF state is unlikely to be stabilized even if U/t is added as a perturbation; this feature is in agreement with that for $U < U_{\rm SF}$ discussed in Sects. 3 and 4.

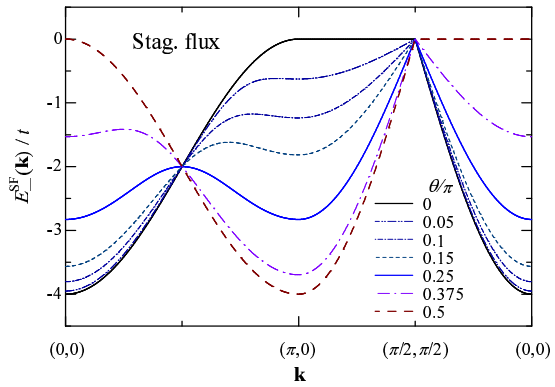

Fig. A·3. (Color online) Energy dispersion of the bare SF state $\Phi_{\rm SF}$ for several values of θ along $(0,0)$-$(\pi,0)$-$(\pi/2,\pi/2)$-$(0,0)$.

The (lower) band structure of the bare SF state, $E_-^{\rm SF}(\mathbf{k})$ [Eq. (A·3)], is shown in Fig. A·3 for several values of θ. In the ordinary Fermi sea ($\theta = 0$), the band top is degenerate along the AF Brillouin zone edge $(\pi,0)$-$(0,\pi)$-$(-\pi,0)$-$(0,-\pi)$, namely, the nesting condition is completely satisfied at half filling. By introducing θ, this degeneracy is lifted and the band top becomes located at $(\pi/2,\pi/2)$ and the three other equivalent points. In particular, for the π-flux state ($\theta = \pi/4$), the band top forms an isotropic Dirac cone centered at $(\pi/2,\pi/2)$. This cone becomes elongated in the $(\pi,0)$-$(0,\pi)$ direction as θ decreases from $\pi/4$.

This peculiar band structure brings about anomalous properties in $\Phi_{\rm SF}$. At half filling, the state for $\theta > 0$ is not a conventional metal. Although it is not explicitly shown here, $n(\mathbf{k})$ is a smooth continuous function except for a discontinuity at $\mathbf{k} = (\pi/2,\pi/2)$, and $N(\mathbf{q}) = S(\mathbf{q})$ becomes a quadratic function of $|\mathbf{q}|$ for $|\mathbf{q}| \to 0$. In a doped case, a Fermi surface appears that is made of a cross section of the elongated Dirac cone near $\mathbf{k} = (\pi/2,\pi/2)$, which is shown in Fig. A·4 for some values of θ and δ and is reminiscent of a Fermi arc or hole pocket observed in cuprates by ARPES and so forth. This is in contrast to the d-SC state Φ_d, in which the Fermi surface is a point on the nodal line irrespective of the value of δ. As δ increases or θ decreases, this segmentary Fermi surface of $\Phi_{\rm SF}$ becomes longer, and the gap region shrinks to the vicinity of the antinodal points. However, the behavior of $N(\mathbf{q})$ [$= S(\mathbf{q})$] for $|\mathbf{q}| \to 0$ in doped $\Phi_{\rm SF}$ is basically unchanged from that at half filling. This gap behavior differs from the case of the *metallic* SF state $\Psi_{\rm SF}$ for $U > U_{\rm SF}$, as discussed in Sects. 3.3

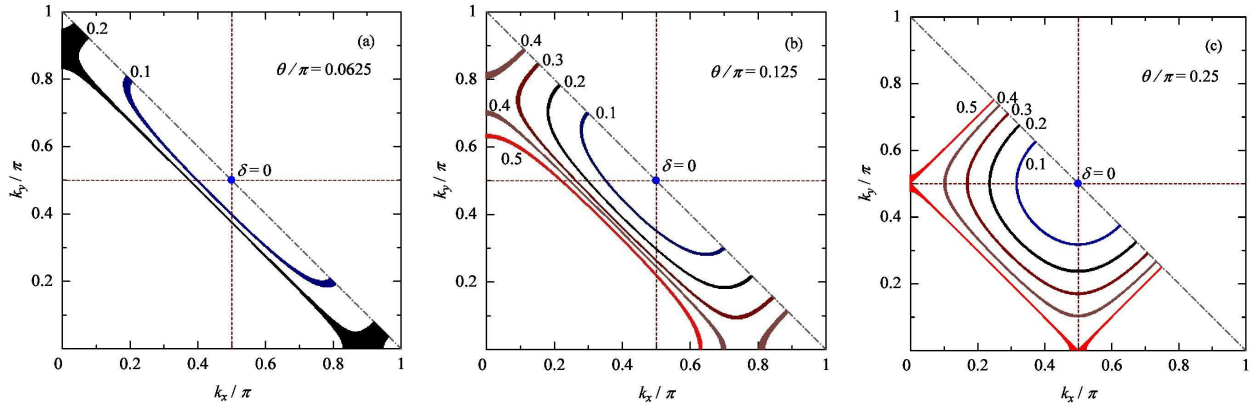

Fig. A·4. (Color online) Fermi surfaces of the bare SF state $\Phi_{\rm SF}$ shown for (a) $\theta = 0.0625$, (b) $\theta = 0.125$, and (c) $\theta = 0.25$ (π flux) for some doping rates. $\mathbf{k}$ points near $\mathbf{k}_{\rm F}$ ($\mathbf{k} \in \mathbf{k}_{\rm F}$) for $L = 1000$ are plotted. The (π, π)-folded Brillouin zone edge is shown by a gray dash-dotted line.

and 4.2.

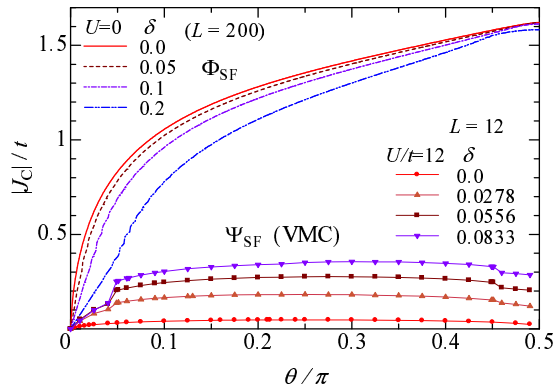

Fig. A·5. (Color online) Local circular currents of one-body SF state ($\Phi_{\rm SF}$) are shown as functions of Peierls phase for four doping rates. The data are numerically computed using Eq. (A·14) for $L = 200$. For comparison, VMC data of $\Psi_{\rm SF}$ for $U/t = 12$ and $L = 12$ are shown for four values of δ.

The local circular current defined by Eq. (18) is calculated for $\Phi_{\rm SF}$ as

$$J_{\rm C} = -\frac{2t\sin\theta}{N_{\rm s}} \sum_{\mathbf{k}\in\mathbf{k}_{\rm F}(\theta),\sigma} \frac{\left(\cos k_x - \cos k_y\right)^2}{\mathcal{S}_{\theta,\mathbf{k}}}, \qquad \text{(A·14)}$$

and is shown in Fig. A·5; the optimal θ is always 0 for the Hubbard model [Fig. A·2(a)]. For comparison, data for strongly correlated cases are also plotted. Here, we only point out two notable features. (i) As δ increases, $|J_{\rm C}|$ decreases for the noninteracting $\Phi_{\rm SF}$, while $|J_{\rm C}|$ increases for the strongly correlated $\Psi_{\rm SF}$ for the Hubbard model with $U/t = 12$. (ii) As the interaction increases, $|J_{\rm C}|$ is markedly reduced.

Appendix B: Staggered Flux State for t-J Model

In this Appendix, we summarize the stability of the SF state in t-J-type models with calculations of reliable accuracy for a comparison with the Hubbard model treated in the main text. For this purpose, we include the following three-site (or pair-hopping) term $\mathcal{H}_{\rm 3site}$, which is the same order as $\mathcal{H}_J$ [t^2/U ($= J/4$)] in the strong-coupling expansion:

$$\mathcal{H}_{t\text{-}J} = \mathcal{H}_t + \mathcal{H}_J, \qquad \mathcal{H}_3 = \mathcal{H}_{t\text{-}J} + \mathcal{H}_{\rm 3site}, \qquad \text{(B·1)}$$

with

$$\mathcal{H}_t = -t \sum_{\langle i,j\rangle,\sigma} \left(\tilde{c}^\dagger_{i\sigma}\tilde{c}_{j\sigma} + \text{H.c.}\right), \qquad \text{(B·2)}$$

$$\mathcal{H}_J = J \sum_{\langle i,j\rangle} \left(\mathbf{S}_i\cdot\mathbf{S}_j - \frac{1}{4}\tilde{n}_i\tilde{n}_j\right), \qquad \text{(B·3)}$$

$$\mathcal{H}_{\rm 3site} = -\frac{J}{4} \sum_{j,\tau\neq\tau',\sigma} \left(\tilde{c}^\dagger_{j,-\sigma}\tilde{c}_{j,-\sigma}\tilde{c}^\dagger_{j+\tau,\sigma}\tilde{c}_{j+\tau',\sigma} + \tilde{c}^\dagger_{j+\tau,-\sigma}\tilde{c}_{j,-\sigma}\tilde{c}^\dagger_{j,\sigma}\tilde{c}_{j+\tau',\sigma}\right), \qquad \text{(B·4)}$$

where $\tilde{c}_{j\sigma} = c_{j\sigma}(1 - n_{j-\sigma})$, $\tilde{n}_j = \sum_\sigma \tilde{c}^\dagger_{j\sigma}\tilde{c}_{j\sigma}$, and $\mathbf{S}_j = \frac{1}{2}\sum_{\alpha,\beta} c^\dagger_{j\alpha}\sigma_{\alpha\beta}c_{j\beta}$ with σ being the Pauli matrix for $S = 1/2$ spins. We call $\mathcal{H}_{t\text{-}J}$ the t-J model and $\mathcal{H}_3$ the three-site model. In doped cases, the behavior of the Hubbard model should be more similar to that of $\mathcal{H}_3$. Here, we disregard diagonal hopping terms for simplicity.

To these models, we apply a VMC scheme similar to that for the Hubbard model. As a many-body factor, we use only the complete Gutzwiller projector, $\mathcal{P} = \mathcal{P}_{\rm G}$ with $g = 0$, as in previous studies.[32,43,44,60] Thus, $\tilde{\Psi}_{\rm SF} = \mathcal{P}_{\rm G}(0)\Phi_{\rm SF}(\theta)$ [$\tilde{\Psi}_{\rm N} = \mathcal{P}_{\rm G}(0)\Phi_{\rm N}$] has one [no] variational parameter. Here, we concentrate on the decrease in energy of $\tilde{\Psi}_{\rm SF}$ from that of $\tilde{\Psi}_{\rm N}$,

$$\tilde{E} = E^{\rm SF}(\theta) - E^{\rm N}, \qquad \text{(B·5)}$$

where $E^{\rm N} = E^{\rm SF}(\theta = 0)$.

First, we consider the half-filled case ($\delta = 0$), in which E_t ($= \langle\mathcal{H}_t\rangle/N_{\rm s}$) and $E_{\rm 3site}$ ($= \langle\mathcal{H}_{\rm 3site}\rangle/N_{\rm s}$) vanish; the total energy is given by the exchange term $E = E_J = \langle\mathcal{H}_J\rangle/N_{\rm s}$. In Fig. B·1, we plot $\tilde{E}_J/J$ ($= \tilde{E}/J$) as a function of θ. $\tilde{E}_J$ has a minimum at $\theta/\pi \sim 0.08$. Because $\tilde{\Psi}_{\rm SF}$ is equivalent to the d-SC state $\tilde{\Psi}_d = \mathcal{P}_{\rm G}\Phi_d$ owing to the SU(2) symmetry,[39,52] the minimum energy of $\tilde{\Psi}_{\rm SF}$ [e.g., $E^{\rm SF}_J/J = -1.1396(4)$ for $L = 10$] coincides with that of $\tilde{\Psi}_d$ [$E^d_J/J = -1.1398$].[32] This value is very low and broadly comparable to the minimum energy of the AF state on the same footing, $\tilde{\Psi}_{\rm AF} = \mathcal{P}_{\rm G}\Psi_{\rm AF}$ [$E^{\rm AF}/J = -1.1412$].[53] Thus, the SF state is very stable at half filling irrespective of the value of J/t.

For doped cases ($\delta > 0$), E_t and $E_{\rm 3site}$ also make contributions. Figure B·2 shows the θ dependence of the three energy components of $\tilde{\Psi}_{\rm SF}$ measured from those of $\tilde{\Psi}_{\rm N}$. By introducing θ, the exchange energy is lowered ($\tilde{E}_J/J < 0$), similarly

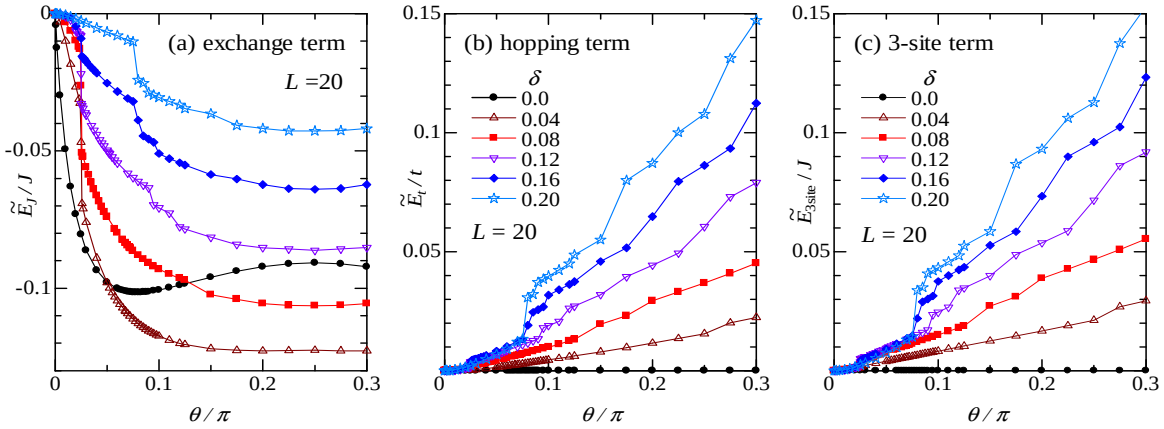

Fig. B·2. (Color online) Energy components of SF state measured from those of $\Psi_{\rm N}$ as functions of θ: (a) exchange term $\langle\mathcal{H}_J\rangle$, (b) hopping term $\langle\mathcal{H}_t\rangle$, and (c) three-site term $\langle\mathcal{H}_{\rm 3site}\rangle$. In each panel, data for several doping rates are plotted. The cusplike foldings appearing for $\delta > 0$ are caused by the discontinuous change in the occupied $\mathbf{k}$-points in $\Phi_{\rm SF}$ as θ varies owing to a finite L.

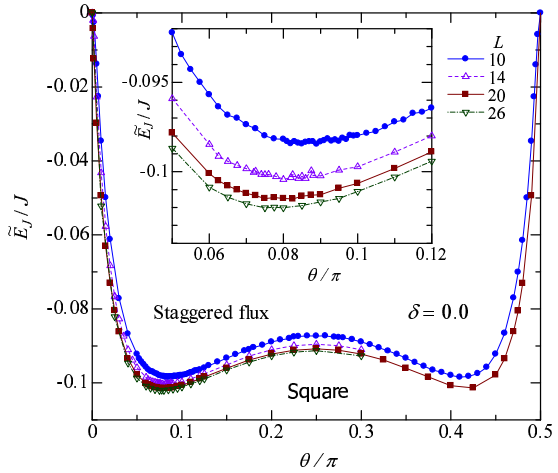

Fig. B·1. (Color online) Exchange energy per site $\tilde{E}_J/J$ of $\tilde{\Psi}_{\rm SF}$ measured from that of $\tilde{\Psi}_{\rm N}$ at half filling as a function of θ. The graph is symmetric with respect to $\theta/\pi = 1/4$ (π-flux). The inset shows the magnification near the minimum ($\theta_{\rm opt}$) of the smaller θ. Data for four values of L are compared.

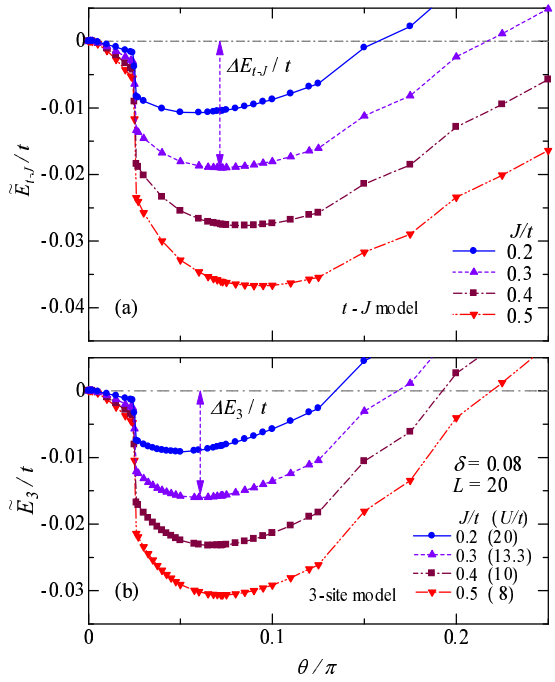

Fig. B·3. (Color online) Total energies of the SF state ($\Psi_{\rm SF}$) measured from that of $\Psi_{\rm N}$ plotted as a function of θ for (a) the t-J model and (b) the three-site model. The doping rate is fixed at 0.08 and the values of J/t are chosen appropriately for cuprates. The values of U/t in (b) are converted using $J = 4t^2/U$. Arrows in both panels indicate the energy gains $\Delta E/t$ by the SF state for $J/t = 0.3$.

to the case of half filling, in a wide range of δ [Fig. B·2(a)]; $|\tilde{E}_J|/t$ is large, especially near half filling. In contrast, $\tilde{E}_t/t$ and $\tilde{E}_{\rm 3site}/J$ monotonically increase with θ, namely, they destabilize the SF state, and become more marked as δ increases [Figs. B·2(b) and B·2(c)]. For fixed values of δ and J/t, the total energy $\tilde{E}/t$ is the sum of these competing components. For example, in Fig. B·3, we plot $\tilde{E}/t$ for the t-J and three-site models for typical values of δ and J/t of underdoped cuprates. We find that $\Psi_{\rm SF}$ is stable with respect to $\Psi_{\rm N}$ in a wide range of J/t. Because $\tilde{E}_{\rm 3site}/J$ is disadvantageous to the SF state [Fig. B·2(c)], the decrease in $\tilde{E}_3/t$ is somewhat smaller than that in $\tilde{E}_{t-J}/t$.

Finally, we look at the δ dependence of the stability of $\tilde{\Psi}_{\rm SF}$. In Fig. B·4(a), we plot the energy gain or difference of $\tilde{\Psi}_{\rm SF}$ as compared with $\tilde{\Psi}_{\rm N}$, defined as

$$\Delta E({\rm SF}) = E({\rm N}) - E({\rm SF}), \qquad \text{(B·6)}$$

for $J/t = 0.3$. Note that ΔE has the inverse sign to $\tilde{E}$. In Fig. B·4(b), we show the optimized θ ($\theta_{\rm opt}$). The behavior of $\theta_{\rm opt}$ is similar to that of $\tilde{E}$, but $\theta_{\rm opt}$ vanishes abruptly at the

size dependence, the range of the SF state seems to expand to some extent in the thermodynamic limit.

Appendix C: Staggered Spin Current State

In this Appendix, we study the staggered spin current (SSC) state $\Psi_{\rm SSC} = \mathcal{P}\Phi_{\rm SSC}$,[40,63,64] as illustrated in Fig. A·1(b). The one-body state, $\Phi_{\rm SSC}$, is obtained as the ground state of the noninteracting SSC model written as

$$\mathcal{H}^{\rm SSC} = -t\sum_{i\in A,\sigma}\Big[e^{i\theta s(\sigma)}\left(c^{\dagger}_{{\rm A}i,\sigma}c_{{\rm B}i,\sigma} + c^{\dagger}_{{\rm A}i,\sigma}c_{{\rm B}i-2\mathbf{x},\sigma}\right)$$

$$+e^{-i\theta s(\sigma)}\left(c^{\dagger}_{{\rm A}i,\sigma}c_{{\rm B}i-\mathbf{x}+\mathbf{y},\sigma} + c^{\dagger}_{{\rm A}i,\sigma}c_{{\rm B}i-\mathbf{x}-\mathbf{y},\sigma}\right) + {\rm H.c.}\Big], \qquad \text{(C·1)}$$

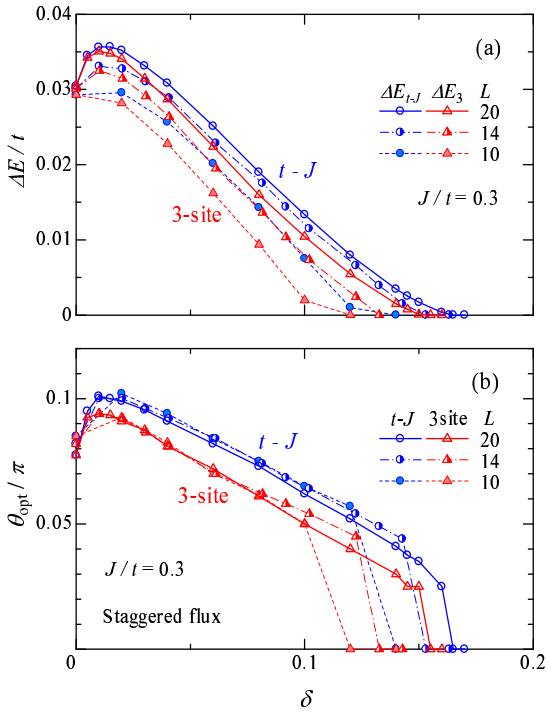

Fig. B·4. (Color online) (a) Doping rate dependence of energy gain of SF state measured from the energy of $\Psi_{\rm N}$ for the t-J (ΔE_2) and the three-site (ΔE_3) models. Data for three values of L are plotted for each model. (b) Optimized values of θ in SF state as functions of doping rate.

where $s(\sigma) = 1$ or -1 according to whether $\sigma = \uparrow$ or $\downarrow$. $\mathcal{H}^{\rm SSC}$ is diagonalized in the same way as $\mathcal{H}^{\rm SF}$. The energy dispersion is identical to $E^{\rm SF}_{\pm}(\mathbf{k})$ [Eq. (A·3)]. Consequently, we have

$$\Phi^{\rm SSC} = \prod_{\mathbf{k}\in\mathbf{k}_{\rm F},\sigma} \frac{1}{\sqrt{2}} \left[\gamma^{\sigma}_{\mathbf{k}}(\theta)\, c^{\dagger}_{A\mathbf{k}\sigma} + c^{\dagger}_{B\mathbf{k}\sigma}\right]|0\rangle, \qquad \text{(C·2)}$$

$$\gamma^{\sigma}_{\mathbf{k}}(\theta) = \frac{e^{-ik_x}\left(e^{i\theta s(\sigma)}\cos k_x + e^{-i\theta s(\sigma)}\cos k_y\right)}{\mathcal{S}_{\theta,\mathbf{k}}}. \qquad \text{(C·3)}$$

$\Phi^{\rm SSC}$ has a doubled unit cell but, in contrast to $\Psi_{\rm SF}$, it has no magnetic flux and preserves the time-reversal symmetry. The SU(2) symmetry is broken in $\Phi^{\rm SSC}$ even at half filling.

For the noninteracting Hubbard model, it is trivial that $\tilde{E}$ [$= E^{\rm SSC}(\theta) - E^{\rm N}$] increases as θ increases because $\Psi_{\rm N}$ is the exact ground state and $E^{\rm SSC}(\theta)$ is equivalent to $E^{\rm SF}(\theta)$ [see Eq. (A·13)]. To consider strongly correlated cases, we apply $\tilde{\Psi}_{\rm SSC} = \mathcal{P}_{\rm G}(0)\Phi_{\rm SSC}$ to the t-J-type model $\langle\mathcal{H}_3\rangle$ in Eq. (B·1) in the same manner as $\tilde{\Psi}_{\rm SF}$ in Appendix B. Figure C·1 shows the θ dependence of the three energy components of $\mathcal{H}_3$. The behavior of $\tilde{E}_t/t$ and $\tilde{E}_3/J$ is similar to that of $\tilde{\Psi}_{\rm SF}$ [Figs. B·2(b) and B·2(c)]. In contrast to $\Psi_{\rm SF}$, however, $\tilde{E}_J/J$ also monotonically increases with θ. The cause of this difference is discussed in Sect. 6.1. Because every component of the energy increases as θ increases, we conclude that $\Psi_{\rm SSC}$ never has a lower energy than $\Psi_{\rm N}$ for $\delta \sim 0$ and positive J/t.

Although we have argued that $\Psi_{\rm SSC}$ is not stabilized in the square-lattice t-J and Hubbard models, a recent VMC study[125] showed that an SSC state has a lower energy than the paramagnetic state for the Heisenberg model on anisotropic triangular lattices with $J' \sim J$ in magnetic fields.[118]

1) For a recent review, see T. Yoshida, M. Hashimoto, I. M. Vishik, Z.-X. Shen, and A. Fujimori, J. Phys. Soc. Jpn. **81**, 011006 (2012).
2) K. Fujita, A. R. Schmidt, E.-A. Kim, M. J. Lawler, D. H. Lee, J. C. Davis, H. Eisaki, and S. Uchida, J. Phys. Soc. Jpn. **81**, 011005 (2012).
3) M. Ogata and H. Fukuyama, Rep. Prog. Phys. **71**, 036501 (2008).
4) P. W. Anderson, P. A. Lee, M. Randeria, T. M. Rice, N. Trivedi, and F. C. Zhang, J. Phys.: Condens. Matter **16**, R755 (2004).
5) J. Zaanen, G. A. Sawatzky, and J. W. Allen, Phys. Rev. Lett. **55**, 418 (1985).
6) M. R. Norman, H. Ding, M. Randeria, J. C. Campuzano, T. Yokoya, T. Takeuchi, T. Takahashi, T. Mochiku, K. Kadowaki, P. Guptasarma, and D. G. Hinks, Nature **392**, 157 (1998).
7) T. Yoshida, X. J. Zhou, T. Sasagawa, W. L. Yang, P. V. Bogdanov, A. Lanzara, Z. Hussain, T. Mizokawa, A. Fujimori, H. Eisaki, Z.-X. Shen, T. Kakeshita, and S. Uchida, Phys. Rev. Lett. **91**, 027001 (2003); T. Yoshida, X. J. Zhou, K. Tanaka, W. L. Yang, Z. Hussain, Z.-X. Shen, A. Fujimori, S. Sahrakorpi, M. Lindroos, R. S. Markiewicz, A. Bansil, S. Komiya, Y. Ando, H. Eisaki, T. Kakeshita, and S. Uchida, Phys. Rev. B **74**, 224510 (2007).
8) N. Doiron-Leyraud, C. Proust, D. LeBoeuf, J. Levallois, J.-B. Bonnemaison, R. Liang, D. A. Bonn, W. N. Hardy, and L. Taillefer, Nature **447**, 565 (2007).
9) N. Barišić, S. Badoux, M. K. Chan, C. Dorow, W. Tabis, B. Vignolle, G. Yu, J. Béard, X. Zhao, C. Proust, and M. Greven, Nat. Phys. **9**, 761 (2013).
10) Studies in this line are broadly classified into two groups: (i) SC fluctuation or precursors to SC and (ii) resonating valence bond (RVB) theory. It was found that the SC fluctuation appears below $T_{\rm pair}$ with $T_{\rm c} < T_{\rm pair} < T^*$ by measurements of the Nernst effect,[11,12] ARPES,[13] and optical conductivity.[14,15] Therefore, the SC fluctuation will not be related to the pseudogap below T^*. In contrast, the RVB mean-field theory successfully explains the pseudogap, particularly, in the spin sector, because the spin degrees of freedom form RVBs, which represent a singlet pairing.[3,4] In this theory, T^* is not a phase-transition temperature but a crossover temperature.
11) L. Li, Y. Wang, S. Komiya, S. Ono, Y. Ando, G. D. Gu, and N. P. Ong, Phys. Rev. B **81**, 054510 (2010).
12) F. Rullier-Albenque, H. Alloul, and G. Rikken, Phys. Rev. B **84**, 014522 (2011).
13) T. Kondo, A. D. Palczewski, Y. Hayama, T. Takeuchi, J. S. Wen, Z. J. Xu, G. Gu, and A. Kaminski, Phys. Rev. Lett. **111**, 157003 (2013).
14) A. Dubroka, M. Rössle, K. W. Kim, V. K. Malik, D. Munzar, D. N. Basov, A. A. Schafgans, S. J. Moon, C. T. Lin, D. Haug, V. Hinkov, B. Keimer, Th. Wolf, J. G. Storey, J. L. Tallon, and C. Bernhard, Phys. Rev. Lett. **106**, 047006 (2011).
15) E. Uykur, K. Tanaka, T. Masui, S. Miyasaka, and S. Tajima, Phys. Rev. Lett. **112**, 127003 (2014).
16) A. Kaminski, S. Rosenkranz, H. M. Fretwell, J. C. Campuzano, Z. Li, H. Raffy, W. G. Cullen, H. You, C. G. Olsonk, C. M. Varma, and H. Höchst, Nature **416**, 610 (2002); A. Shekhter, B. J. Ramshaw, R. Liang, W. N. Hardy, D. A. Bonn, F. F. Balakirev, R. D. McDonald, J. B. Betts, S. C. Riggs, and A. Migliori, Nature **498**, 75 (2013).
17) B. Fauqué, Y. Sidis, V. Hinkov, S. Pailhès, C. T. Lin, X. Chaud, and P. Bourges, Phys. Rev. Lett. **96**, 197001 (2006).
18) V. Balédent, B. Fauqué, Y. Sidis, N. B. Christensen, S. Pailhès, K. Conder, E. Pomjakushina, J. Mesot, and P. Bourges, Phys. Rev. Lett. **105**, 027004 (2010).
19) Y. Li, V. Balédent, N. Barišić, Y. Cho, B. Fauqué, Y. Sidis, G. Yu, X. Zhao, P. Bourges, and M. Greven, Nature **455**, 372 (2008); Y. Li, V. Balédent, G. Yu, N. Barišić, K. Hradil, R. A. Mole, Y. Sidis, P. Steffens, X. Zhao, P. Bourges, and M. Greven, Nature **468**, 283 (2010); Y. Li, G. Yu, M. K. Chan, V. Balédent, Y. L. N. Barišić, X. Zhao, K. Hradil, R. A. Mole, Y. Sidis, P. Steffens, P. Bourges, and M. Greven, Nat. Phys. **8**, 404 (2012).
20) M. Fujita, H. Hiraka, M. Matsuda, M. Matsuura, J. M. Tranquada, S. Wakimoto, G. Xu, and K. Yamada, J. Phys. Soc. Jpn. **81**, 011007 (2012).
21) G. Ghiringhelli, M. Le Tacon, M. Minola, S. Blanco-Canosa, C. Mazzoli, N. B. Brookes, G. M. De Luca, A. Frano, D. G. Hawthorn, F. He,

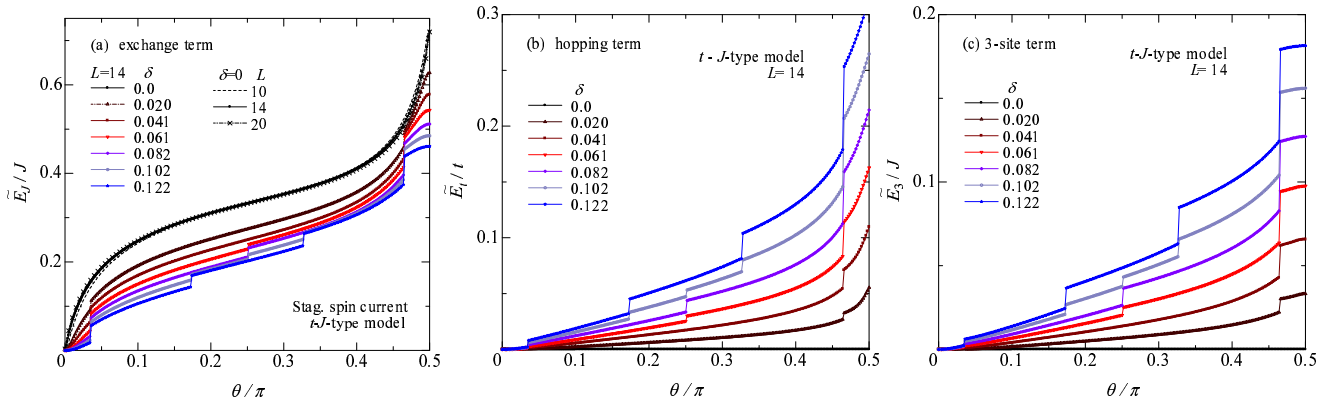

Fig. C·1. (Color online) Energy components of staggered spin current state measured from those of $\Psi_N = \Psi_{SSC}(\theta = 0)$, similarly to in Fig. B·2. In (a), data for three values of L are compared at half filling to show the small finite-size effect.

G. A. Sawatzky, E. Weschke, B. Keimer, and L. Braicovich, Science **337**, 821 (2012).

22) J. Chang, E. Blackburn, A. T. Holmes, N. B. Christensen, J. Larsen, J. Mesot, R. Liang, D. A. Bonn, W. N. Hardy, A. Watenphul, M. v. Zimmermann, E. M. Forgan, and S. M. Hayden, Nat. Phys. **8**, 871 (2012).
23) A. J. Achkar, R. Sutarto, X. Mao, F. He, A. Frano, S. Blanco-Canosa, M. Le Tacon, G. Ghiringhelli, L. Braicovich, M. Minola, M. M. Sala, C. Mazzoli, R. Liang, D. A. Bonn, W. N. Hardy, B. Keimer, G. A. Sawatzky, and D. G. Hawthorn, Phys. Rev. Lett. **109**, 167001 (2012).
24) K. Nakayama, T. Sato, T. Dobashi, K. Terashima, S. Souma, H. Matsui, T. Takahashi, J. C. Campuzano, K. Kudo, T. Sasaki, N. Kobayashi, T. Kondo, T. Takeuchi, K. Kadowaki, M. Kofu, and K. Hirota, Phys. Rev. B **74**, 054505 (2006).
25) S. E. Sebastian, N. Harrison, E. Palm, T. P. Murphy, C. H. Mielke, R. Liang, D. A. Bonn, W. N. Hardy, and G. G. Lonzarich, Nature **454**, 200 (2008).
26) E. Razzoli, Y. Sassa, G. Drachuck, M. Mansson, A. Keren, M. Shay, M. H. Berntsen, O. Tjernberg, M. Radovic, J. Chang, S. Pailhès, N. Momono, M. Oda, M. Ido, O. J. Lipscombe, S. M. Hayden, L. Patthey, J. Mesot, and M. Shi, New J. Phys. **12**, 125003 (2010).
27) R.-H. He, X. J. Zhou, M. Hashimoto, T. Yoshida, K. Tanaka, S.-K. Mo, T. Sasagawa, N. Mannella, W. Meevasana, H. Yao, M. Fujita, T. Adachi, S. Komiya, S. Uchida, Y. Ando, F. Zhou, Z. X. Zhao, A. Fujimori, Y. Koike, K. Yamada, Z. Hussain, and Z.-X. Shen, New J. Phys. **13**, 013031 (2011).
28) For instance, Y. H. Liu, Y. Toda, K. Shimatake, N. Momono, M. Oda, and M. Ido, Phys. Rev. Lett. **101**, 137003 (2008).
29) J. L. Tallon, F. Barber, J. G. Strey, and J. W. Loram, Phys. Rev. B **87**, 140508 (2013).
30) T. Yoshida, W. Malaeb, S. Ideta, D. H. Lu, R. G. Moor, Z.-X. Shen, M. Okawa, T. Kiss, K. Ishizaka, S. Shin, S. Komiya, Y. Ando, H. Eisaki, S. Uchida, and A. Fujimori, Phys. Rev. B **93**, 014513 (2016).
31) H. Yokoyama and H. Shiba, J. Phys. Soc. Jpn. **57**, 2482 (1988); C. Gros, Ann. Phys. (New York) **189**, 53 (1989).
32) H. Yokoyama and M. Ogata, J. Phys. Soc. Jpn. **65**, 3615 (1996).
33) H. Yokoyama, Y. Tanaka, M. Ogata, and H. Tsuchiura, J. Phys. Soc. Jpn. **73**, 1119 (2004).
34) H. Yokoyama, M. Ogata, and Y. Tanaka, J. Phys. Soc. Jpn. **75**, 114706 (2006).
35) H. Yokoyama, M. Ogata, Y. Tanaka, K. Kobayashi, and H. Tsuchiura, J. Phys. Soc. Jpn. **82**, 014707 (2013).
36) A. Paramekanti, M. Randeria, and N. Trivedi, Phys. Rev. B **70**, 054504 (2004).
37) D. Tahara and M. Imada, J. Phys. Soc. Jpn. **77**, 114701 (2008).
38) R. Sato and H. Yokoyama, J. Phys. Soc. Jpn. **85**, 074701 (2016).
39) I. Affleck and J. B. Marston, Phys. Rev. B **37**, 3774 (1988).
40) H. J. Schulz, Phys. Rev. B **39**, 2940 (1989).
41) P. Lederer, D. Poilblanc, and T. M. Rice, Phys. Rev. Lett. **63**, 1519 (1989); D. Poilblanc and Y. Hasegawa, Phys. Rev. B **41**, 6989 (1990).
42) F. C. Zhang, Phys. Rev. Lett. **64**, 974 (1990).
43) S. Liang and N. Trivedi, Phys. Rev. Lett. **64**, 232 (1990).
44) T. K. Lee and L. N. Chang, Phys. Rev. B **42**, 8720 (1990).
45) M. Ogata, B. Douçot, and T. M. Rice, Phys. Rev. B **43**, 5582 (1991).
46) P. A. Lee and X.-G. Wen, Phys. Rev. B **63**, 224517 (2001).
47) J. Kishine, P. A. Lee, and X.-G. Wen, Phys. Rev. Lett. **86**, 5365 (2001).
48) Q.-H. Wang, J. H. Han, and D.-H. Lee, Phys. Rev. Lett. **87**, 167004 (2001).
49) H. Tsuchiura, M. Ogata, Y. Tanaka, and S. Kashiwaya, Phys. Rev. B **68**, 012509 (2003).
50) T. Kuribayashi, H. Tsuchiura, Y. Tanaka, J. Inoue, M. Ogata, and S. Kashiwaya, Physica C **392-396**, 419 (2003).
51) I. Affleck, Z. Zou, T. Hsu, and P. W. Anderson, Phys. Rev. B **38**, 745 (1988).
52) F. C. Zhang, C. Gros, T. M. Rice, and H. Shiba, Supercond. Sci. Technol. **1**, 36 (1988).
53) H. Yokoyama and H. Shiba, J. Phys. Soc. Jpn. **56**, 3570 (1987).
54) N. Trivedi and D. Ceperley, Phys. Rev. B **40**, 2737 (1989).
55) K. J. Runge, Phys. Rev. B **45**, 12292 (1992).
56) M. U. Ubbens and P. A. Lee, Phys. Rev. B **46**, 8434 (1992).
57) X.-G. Wen and P. A. Lee, Phys. Rev. Lett. **76**, 503 (1996); P. A. Lee, N. Nagaosa, T.-K. Ng, and X.-G. Wen, Phys. Rev. B **57**, 6003 (1998).
58) K. Hamada and D. Yoshioka, Phys. Rev. B **67**, 184503 (2003).
59) E. Cappelluti and R. Zeyher, Phys. Rev. B **59**, 6475 (1999).
60) D. A. Ivanov and P. A. Lee, Phys. Rev. B **68**, 132501 (2003).
61) D. A. Ivanov, Phys. Rev. B **70**, 104503 (2004).
62) S. Chakravarty, R. B. Laughlin, D. K. Morr, and C. Nayak, Phys. Rev. B **63**, 094503 (2001).
63) A. A. Nersesyan, G. I. Japaridze, and I. G. Kimeridze, J. Phys.: Condens. Matter **3**, 3353 (1991).
64) M. Ozaki, Int. J. Quantum Chem. **42**, 55 (1992).
65) B. Normand and A. M. Oleś, Phys. Rev. B **70**, 134407 (2004).
66) B. Binz, D. Baeriswyl, and B. Douçot, Eur. Phys. J. B **25**, 69 (2002).
67) C. Honerkamp, M. Salmhofer, and T. M. Rice, Eur. Phys. J. B **27**, 127 (2002). The tendency of these RG results seems consistent with the present results.
68) T. D. Stanescu and P. Phillips, Phys. Rev. B **64**, 220509 (2001).
69) A. Macridin, M. Jarrell, and T. Maier, Phys. Rev. B **70**, 113105 (2004).
70) X. Lu, L. Chioncel, and E. Arrigoni, Phys. Rev. B **85**, 125117 (2012).
71) J. Otsuki, J. Hafermann, and A. I. Lichtenstein, Phys. Rev. B **90**, 235132 (2014).
72) S. Tamura and H. Yokoyama, J. Phys. Soc. Jpn. **84**, 064707 (2015).
73) A. Ardavan, S. Brown, S. Kagoshima, K. Kanoda, K. Kuroki, H. Mori, M. Ogata, S. Uji, and J. Wosnitza, J. Phys. Soc. Jpn. **81**, 011004 (2012).
74) H. Mayaffre, P. Wzietek, C. Lenoir, D. Jérome, and P. Batail, Europhys. Lett. **28**, 205 (1994).
75) B. J. Powell and R. H. McKenzie, Rep. Prog. Phys. **74**, 056501 (2011).
76) H. Kino and H. Fukuyama, J. Phys. Soc. Jpn. **65**, 2158 (1996).
77) Y. Shimizu, M. Maesato, and G. Saito, J. Phys. Soc. Jpn. **80**, 074702 (2011).
78) Y. Shimizu, H. Kasahara, T. Furuta, K. Miyagawa, K. Kanoda,

M. Maesato, and G. Saito, Phys. Rev. B **81**, 224508 (2010).
79) Y. Eto, M. Itaya, and A. Kawamoto, Phys. Rev. B **81**, 212503 (2010).
80) H. Yokoyama, S. Tamura, and M. Ogata, JPS Conf. Proc. **3**, 012029 (2014).
81) H. Yokoyama, S. Tamura, T. Watanabe, K. Kobayashi, and M. Ogata, Phys. Proc. **58**, 14 (2014).
82) T. Tohyama and S. Maekawa, Supercond. Sci. Technol. **13**, R17 (2000).
83) H. Shiba and M. Ogata, J. Phys. Soc. Jpn. **59**, 2971 (1990).
84) M. C. Gutzwiller, Phys. Rev. Lett. **10**, 159 (1963).
85) T. A. Kaplan, P. Horsch, and P. Fulde, Phys. Rev. Lett. **49**, 889 (1982).
86) H. Yokoyama and H. Shiba, J. Phys. Soc. Jpn. **59**, 3669 (1990).
87) A. J. Millis and S. N. Coppersmith, Phys. Rev. B **43**, 13770 (1991).
88) Precisely speaking, θ in the wave function slightly deviates from the actually averaged value of the phase variation $\langle\theta\rangle$ in the hopping processes as in Fig. 3. At half filling, $\langle\theta\rangle$ is slightly larger than θ but $\theta \sim \langle\theta\rangle$ holds as a whole. For a sufficiently large U/t, $\phi = \langle\theta\rangle$ holds rather than $\phi = \theta$.
89) In this process, a phase assignment similar to Eq. (12), such as
$$\mathcal{P}_\xi = \exp\left\{ i\xi \sum_j (-1)^j h_j \left[\prod_\tau \left(1 - d_{j+\tau}\right) \right] \left(n_{j+x} + n_{j-x} - n_{j+y} - n_{j-y}\right) \right\},$$
can be assumed, where $n_j = n_{j\uparrow} + n_{j\downarrow}$ and ξ is a variational parameter. However, we can easily show that $\mathcal{P}_\xi = 1$, namely, the phase variation θ in the hopping of isolated holons is not controlled by this type of phase factor.
90) C. Weber, A. Läuchli, F. Milla, and T. Giamarchi, Phys. Rev. Lett. **102**, 017005 (2009).
91) If we apply $\mathcal{P}_\phi$ to a real wave function such as $\Psi_{\rm N}$, $\Psi_{\rm AF}$, or Ψ_d, the phase factor in $\mathcal{P}_\phi$ is optimized as $\phi = 0$, namely, $\mathcal{P}_\phi = 1$. Therefore, expectation values associated with the optimized real state do not alter regardless of whether $\mathcal{P}_\phi$ is introduced or not.
92) Y. Toga and H. Yokoyama, Phys. Proc. **65**, 29 (2015).
93) S. Tamura and H. Yokoyama, Phys. Proc. **81**, 5 (2016).
94) W. L. McMillan, Phys. Rev. **138**, A442 (1965).
95) D. Ceperley, G. V. Chester, and D. H. Kalos, Phys. Rev. B **16**, 3081 (1977).
96) H. Yokoyama and H. Shiba, J. Phys. Soc. Jpn. **56**, 1490 (1987).
97) C. J. Umrigar, K. G. Wilson, and J. W. Wilkins, Phys. Rev. Lett. **60**, 1719 (1988).
98) Because the band-renormalization effect[99] is small in $\Psi_{\rm AF}$ as well as in Ψ_d even for $\delta \sim 0$ (See Ref. 38) in the case of $t' = 0$, we do not treat it here. It does not directly affect the present result.
99) A. Himeda and M. Ogata, Phys. Rev. Lett. **85**, 4345 (2000).
100) To estimate $U_{\rm c}/t$ more accurately, the long-range part of the D-H (Jastrow) factor is important.[101,102] Therefore, here we do not pursue the quantitative accuracy of $U_{\rm c}/t$.
101) M. Capello, F. Becca, M. Fabrizio, S. Sorella, and E. Tosatti, Phys. Rev. Lett. **94**, 026406 (2005).
102) T. Miyagawa and H. Yokoyama, J. Phys. Soc. Jpn. **80**, 084705 (2011).
103) R. P. Feynman, *Statistical Mechanics* (Benjamin/Cummings, Reading, MA., 1972) Chap. 11; A. Auerbach, *Interacting Electrons and Quantum Magnetism* (Springer, New York, 1974) Chap. 9.
104) For a procedure of applying SMA to finite-size systems, see, for instance, the treatment in constructing Fig. 5 in Ref. 105, in which a conductive spin-gap state was similarly confirmed in the Bose-Einstein-condensation regime for the attractive Hubbard model.
105) S. Tamura and H. Yokoyama, J. Phys. Soc. Jpn. **81**, 064718 (2012).
106) To examine the behavior of $S(\mathbf{q})$ for $|\mathbf{q}| \to 0$, we consider the second-order finite difference for L calculated using the smallest three $|\mathbf{q}|$ points in the x direction:
$$C(L) = \frac{\Delta^2 S(\mathbf{q})}{\Delta|\mathbf{q}|^2} = \frac{S(0,0) + S(4\pi/L, 0) - 2S(2\pi/L, 0)}{(2\pi/L)^2}.$$
If $C(L)$ is positive for $L \to \infty$, $S(\mathbf{q})$ is a quadratic (or higher-order) function, whereas if $|C(\infty)|$ vanishes, $S(\mathbf{q})$ becomes a linear function. For a typical value of the spin-gap metal phase [$U/t = 6.5$; brown symbols in the inset in Fig. 8(c)], $C(L)$ becomes 0.154, 0.203, 0.232, and 0.257 for $L = 10$, 12, 14, and 16, respectively. $C(L)$ is an increasing function of L and likely to remain positive for $L \to \infty$. This tendency also holds for the Mott insulating regime ($U > U_{\rm c}$). In contrast, for a typical Fermi liquid [$U/t = 4$; black symbols in the inset in Fig. 8(c)], $|C(L)|$ with $C(L) < 0$ tends to decrease as L increases, suggesting that $S(\mathbf{q})$ is linear.
107) At half filling, the occupied $\mathbf{k}$ points (within the magnetic Brillouin zone) do not alter as U/t varies; the SF transition tends toward a continuous transition as L increases. In a doped case with finite L, however, the occupied $\mathbf{k}$ points suddenly change as θ changes at several values of θ ($= \theta_{\rm a}, \theta_{\rm b}, \cdots$). Consequently, ΔE becomes a discontinuous function of θ with multiple local minima. Thus, the optimized θ switches, for instance, from θ_1 ($0 \le \theta_1 < \theta_{\rm a}$) to θ_2 ($\theta_{\rm a} \le \theta_2 < \theta_{\rm b}$) at certain values of U/t. The present SF transition for finite L corresponds to a first-order transition from θ_1 ($= 0$) to θ_2 (> 0). However, because the change in the Fermi surface becomes continuous as $L \to \infty$, the SF transition is expected to become a continuous transition in this limit.
108) In the t-J model, not only $\delta_{\rm SF}$ but also δ_d (the transition point from Ψ_d to $\Psi_{\rm N}$) tends to be large as compared with in the Hubbard model.
109) In Fig. 16, we find that the system-size dependence becomes large when δ approaches $\delta_{\rm SF}$. This is because the optimal θ discontinuously switches from the lower edge of the second continuous segment ($\theta_{\rm a}$ in Ref. 107) to zero (minimum in the first segment) at $U = U_{\rm SF}$. The value of $\theta_{\rm a}$ depends on L; $\theta_{\rm a} \to 0$ as $L \to \infty$.
110) Here, $U_{\rm SF}/t$ is estimated without considering the band renormalization in $\Psi_{\rm N}$ for ease of calculation; therefore, the area of the SF state may shrink to some extent near half filling.
111) X. G. Wen, F. Wilczek, and A. Zee, Phys. Rev. B **39**, 11413 (1989).
112) K. Kobayashi and H. Yokoyama, JPS Conf. Proc. **1**, 012120 (2014); JPS Conf. Proc. **3**, 015012 (2014); Phys. Proc. **58**, 22 (2014); Phys. Proc. **65**, 9 (2015).
113) T. Misawa and M. Imada, Phys. Rev. B **90**, 115137 (2014).
114) H. Yokoyama, R. Sato, S. Tamura, and M. Ogata, Phys. Proc. **65**, 29 (2015).
115) T. Watanabe, H. Yokoyama, Y. Tanaka, and J. Inoue, J. Phys. Soc. Jpn. **75**, 074707 (2006); Phys. Rev. B **77**, 214505 (2008).
116) L. F. Tocchio, H. Feldner, F. Becca, R. Valentí, and C. Gros, Phys. Rev. B **87**, 035143 (2013).
117) L. F. Tocchio, A. Parola, C. Gros, and F. Becca, Phys. Rev. B **80**, 064419 (2009).
118) For instance, S. Fujimoto, Phys. Rev. Lett. **106**, 196407 (2011); A. V. Chubkov and O. A. Starykh, Phys. Rev. Lett. **110**, 217210 (2013).
119) Generally, the band renormalization also occurs so as to reduce the kinetic energy.[38] In Fig. 20, we show the boundary where the effective band in $\Psi_{\rm N}$ is renormalized to $t_1 = 0$ and then the nesting condition, which is lost for $t' \neq 0$, is restored. Note that this boundary for $t'/t \gtrsim 0.3$ behaves similarly to the phase boundary between $\Psi_{\rm N}$ and $\Psi_{\rm SF}$ of concern in the text.
120) J. D. Sau, I. Mandal, S. Tewari, and S. Chakravarty, Phys. Rev. B **87**, 224503 (2013).
121) C. M. Varma, Phys. Rev. B **55**, 14554 (1997); Phys. Rev. B **73**, 155113 (2006).
122) C. Weber, T. Giamarchi, and C. Varma, Phys. Rev. Lett. **101**, 017001 (2014).
123) S. Tamura, Dr. Thesis, Faculty of Science, Tohoku University, Sendai (2016) [in Japanese].
124) In this connection, we mention the renormalization flow in $\Psi_{\rm N}$. As in Fig. 19(a), $t_1 < t'$ holds and the value of $t'_{\rm c2}/t$ at $U/t = 8$ decreases as L increases for $t'/t \lesssim 0.8$, indicating that the flow is directed to $t'/t \to 0$ in this regime. On the other hand, we find that $t_1 > t'$ for $t'/t \gtrsim 1.3$ and $t'_{\rm c2}/t$ increases with L at $U/t = 12$, meaning that the flow is directed to $t'/t \to \infty$. Similar analysis has been performed for a paramagnetic state in the Heisenberg model ($U/t \to \infty$) on an anisotropic triangular lattice, and it was concluded that the boundary is $J'/J \sim 0.95$.[125]
125) S. Tamura and H. Yokoyama, Phys. Proc. **58**, 10 (2014).
126) K.-Y. Yang, T. M. Rice, and F.-C. Zhang, Phys. Rev. B **73**, 174501 (2006).
127) Y. Sidis, C. Ulrich, P. Bourges, C. Bernhard, C. Niedermayer, L. P. Regnault, N. H. Andersen, and B. Keimer, Phys. Rev. Lett. **86**, 4100 (2001); H. A. Mook, P. Dai, S. M. Hayden, A. Hiess, J. W. Lynn, S.-H. Lee, and F. Doğan, Phys. Rev. B **66**, 144513 (2002); J. A. Hodges, Y. Sidis, P. Bourges, I. Mirebeau, M. Hennion, and X. Chaud, Phys. Rev. B **66**, 020501(R) (2002).
128) We should rectify the argument in Refs. 80 and 81 that the SF state may be an underlying normal state from which d-SC arises.

130) In electron-doped cuprates, pseudogap behavior has been found at the so-called hot spots—the intersections of a quasi-Fermi surface with the AF-Brillouin-zone boundary—, which are detached from the antinodal points.[131] This pseudogap is related to AF correlations[132] or AF orders.[133] The *d*-SC gap also has a maximum at the hot spot.[134] However, recent experiments on high-quality samples showed that such an AF pseudogap is suppressed.[135]
131) N. P. Armitage, D. H. Lu, C. Kim, A. Damascelli, K. M. Shen, F. Ronning, D. L. Feng, P. Bogdanov, Z.-X. Shen, Y. Onose, Y. Taguchi, Y. Tokura, P. K. Mang, N. Kaneko, and M. Greven, Phys. Rev. Lett. **87**, 147003 (2001).
132) Y. Onose, Y. Taguchi, K. Ishizaka, and Y. Tokura, Phys. Rev. Lett. **87**, 217001 (2001).
133) H. Matsui, K. Terashima, T. Sato, T. Takahashi, S.-C. Wang, H.-B. Yang, H. Ding, T. Uefuji, and K. Yamada, Phys. Rev. Lett. **94**, 047005 (2005).
134) H. Matsui, K. Terashima, T. Sato, T. Takahashi, M. Fujita, and K. Yamada, Phys. Rev. Lett. **95**, 017003 (2005).
135) M. Horio, T. Adachi, Y. Mori, A. Takahashi, T. Yoshida, H. Suzuki, L. C. C. Ambolode II, K. Okazaki, K. Ono, H. Kumigashira, H. Anzai, M. Arita, H. Namatame, M. Taniguchi, D. Ootsuki, K. Sawada, M. Takahashi, T. Mizokawa, Y. Koike, and A. Fujimori, Nat. Commun. **7**, 10567 (2016).
136) R. B. Laughlin, Phys. Rev. B **89**, 035134 (2014).